

Optimizing Experimental Parameters for Orbital Mapping

Manuel Ederer^a, Stefan Löffler^a

^aUniversity Service Centre for Transmission Electron Microscopy, TU Wien, Wiedner Hauptstraße 8-10/E057-02, 1040 Wien, Austria

Abstract

A new material characterization technique is emerging for the transmission electron microscope (TEM). Using electron energy-loss spectroscopy, real space mappings of the underlying electronic transitions in the sample, so called orbital maps, can be produced. Thus, unprecedented insight into the electronic orbitals responsible for most of the electrical, magnetic and optical properties of bulk materials can be gained. However, the incredibly demanding requirements on spatial as well as spectral resolution paired with the low signal-to-noise ratio severely limits the day-to-day use of this new technique. With the use of simulations, we strive to alleviate these challenges as much as possible by identifying optimal experimental parameters. In this manner, we investigate representative examples of a transition metal oxide, a material consisting entirely of light elements, and an interface between two different materials to find and compare acceptable ranges for sample thickness, acceleration voltage and electron dose for a scanning probe as well as for parallel illumination.

Keywords: transmission electron microscopy, electron energy-loss spectroscopy, orbital mapping, rutile, graphite, SrTiO₃-LaMnO₃

1. Introduction

The wheel of technological progress is ever turning. Improvements to aberration correctors, electron detectors and spectrometers allow us to push spatial and energy resolution to continually smaller boundaries. Atomic resolution is now routinely achieved for both fixed-beam and scanning transmission electron microscopy (STEM) for many years [1]. Even coupled with electron-energy loss spectroscopy (EELS) [2, 3, 4] or energy dispersive x-ray (EDX) analysis [5, 6, 7], atomic resolution is now possible in the resulting energy-filtered maps. With orbital mapping [8, 9, 10], however, we strive to fly even closer to the sun. Contrary to elemental mapping, a tiny energy window of often less than 2 eV is necessary. This ensures that not the whole ionization edge is used for mapping, but only a single peak or feature of the energy loss near edge structure (ELNES), thus allowing us to map an electronic transition between specific orbitals in the sample material. In

many cases, this procedure is equivalent to imaging the spatial distribution of originally unoccupied electronic orbitals near Fermi level. Thus, using this method allows to get a peak at the individual electronic orbitals directly responsible for basically all electronic and magnetic properties and chemical binding of a given material. Up to recently, this was only possible for states located at the material surface through scanning tunneling microscopy [11, 12, 13]. Using a TEM, however, orbital mapping of bulk materials becomes possible. In principle, this allows the investigation of any region of interest in the material such as defects or internal boundaries between different phases or materials. However, the demanding needs for high spatial and spectral resolution coupled with the extremely low signal-to-noise ratio due to the tiny energy windows limit the broad applicability of this promising new method for now. Thus, it is of paramount importance to overcome these limitations by optimizing all other, more freely chooseable experimental imaging parameters such as sample thickness, acceleration voltage and electron incidence dose.

Email address: manuel.ederer@tuwien.ac.at (Manuel Ederer)

Aided by density functional theory and electron channelling simulations, our goal in this work is to find the perfect set of experimental parameters for three material classes: transition metal oxides (by the example of rutile), materials made up of light elements (by the example of graphite), and interfaces (by the example of the SrTiO₃-LaMnO₃ heterostructure). If there exists no perfect set we will settle for parameter ranges that produce still acceptable orbital maps. Acceptability is gauged as objectively as possible by the use of an image difference metric and the resulting difference relative to a perfect reference image [14, 15, 16]. We have chosen rutile and graphite as their electronic structure makes these materials particularly suitable for orbital mapping while their crystal structure is still relatively simple. Further, they provide the opportunity to study the effects of elastic scattering on the resulting orbital maps, as graphite consists only of light atoms while rutile consists of both light and relatively heavy atoms. The SrTiO₃-LaMnO₃ heterostructure, in particular the region at/around the interface, has been chosen due to its, in comparison, complex structure and as a potential application. Mapping core loss transitions in the vicinity of material defects and interfaces allows for potentially unrivaled insight into the local electronic and magnetic properties of the material [9].

While up to now, experimental orbital maps have only been reported using scanning TEM, using EFTEM should be equally possible [17]. Thus, we will simulate images both for a scanning probe as well as for parallel illumination. This allows us to compare acceptable parameter ranges between STEM and energy-filtered TEM (EFTEM) for orbital mapping whenever a direct comparison is possible.

2. Methods

We calculate theoretical orbital maps by employing the multislice algorithm [18, 19] for the elastic propagation of the probe electron through the sample material. The inelastic interaction between probe electrons and sample electrons is calculated with the mixed dynamic form factor [17, 20, 21] based on density functional theory data obtained with WIEN2k [22]. Energy filtering and subsequent mapping allows us to image the corresponding transition in real space [8, 9]. The energy window will

be chosen infinitely small for this work in order to decrease the numerical work load and will consist only of a single energy point. Further, we focus only on core loss transitions, in particular on K and L edges, and interpret the resulting image as the spatial representation of the originally unoccupied orbital in the conduction band. EFTEM images are simulated by assuming an incidental plane wave. STEM spectrum images, however, require an entire multislice calculation for each pixel with the convergent electron beam centered at the pixel's position. Thus, even when taking parallel execution into account, the STEM simulations result in often restrictively long computation times.

For each material, we perform simulations for a representative range of sample thicknesses. The thinnest samples are only a single unit cell thick and result, for infinite electron dose, in the qualitatively best image. For relatively thick samples (60 – 100 unit cells), we are unfortunately quickly limited by the aforementioned STEM computation times, which is also the reason for the varying thickest samples for different materials. Nonetheless, for the thickness-dose investigations, we have successfully managed to include selected simulations of samples thicker than 20 nm for all materials.

We perform these thickness-dose investigations by including shot noise in the resulting images. By keeping a constant ratio between the electron counts in the image and the thickness dependent signal intensity, we effectively simulate a certain electron incident dose. Thus, without knowing the relation between the absolute electron incident dose and the resulting image dose, we can still give the relative incident dose and calculate the specific electron counts from a given reference case. This allows us to provide a more realistic comparison between different sample thicknesses than it would be the case for infinite dose.

In order to automate and objectify the evaluation of the image for a specific parameter set, we employ an image difference metric suitable for TEM [23] based on the scale invariant feature transform (SIFT) algorithm [24]. This method detects features in a reference image and compares their orientation and image gradient to the features at the same positions in any given image of interest. Based on these differences, a total image difference is assigned to the image pair. An image difference of 0 hereby indicates identical images and 1 the maximal achievable difference to the reference image. The parameters for the respective reference images are given

in Tab. 2.

The method is especially well suited for orbital mapping, as the optimal image can easily be calculated for infinite electron dose and a projected sample thickness of a single unit cell. For STEM, we have chosen $\alpha = 30$ mrad and $\beta = 50$ mrad, as these values result in highly detailed orbital maps while still being reasonably achievable in the experiment. Similarly, step sizes have been chosen to allow for enough pixels per feature (orbital), so that image difference detection still performs reliably, while not too far away from typical experimental values. Additionally, step sizes in x and y direction are different (except for rutile). We have chosen them with the restriction that the resulting pixels per unit cell are an integer number in order to avoid artifacts. For all simulated images, spherical aberration and incoherent source size broadening were neglected.

We have chosen two thresholds to further categorize the resulting image difference number, based on investigations of nano particle detectability using the SIFT metric [23]. Below a value of 0.18, the images that are compared can for all practical purposes be considered as identical for current state-of-the-art TEMs and the parameter set resulting in the image as optimal. Images with difference values up to 0.3, while exhibiting already significant deviations to the reference image, still contain enough of the underlying orbital information for the parameter set to be considered acceptable here. Accordingly, we will mark these thresholds in the relevant figures throughout this work with dark green and olive coloured contour lines or backgrounds. We begin with an investigation of the relevant parameters for STEM-EELS and EFTEM separately. Afterwards, we compare the methods if possible and evaluate their respective theoretical capability of achieving orbital mapping.

3. Materials and Results

3.1. Rutile

The rutile phase of TiO_2 is a prime target for orbital mapping due to its crystal field induced splitting of its unoccupied states near the Fermi level into t_{2g} -like and e_g -like bands [25, 26, 27, 28]. A large enough energetic separation of final states in the conduction band is crucial for orbital mapping as otherwise individual transitions to final states

with different angular momentum character overlap in the resulting image. Subsequently, all directional information of the orbital map would be lost according to Unsöld's theorem [29]. In the past, the t_{2g} transitions of Ti have already been successfully mapped in a proof of principle work of Löffler et al. [8] and more recently reproduced by Oberaigner et al. [30].

The O K-edge yields two different relevant orbital maps, both with a characteristic dumbbell shape for the chosen projection along the $[001]$ zone axis, due to the underlying electronic transition to a final state with p angular momentum character [17]. The resulting mapped orbitals are either aligned in the direction towards the nearest Ti neighbour atom or perpendicular to the direction and will be defined as p_x and p_y , respectively. The specific energy losses of the two cases, 535.9 eV for p_x and 539 eV for p_y , have been chosen based on the projected density of states (pDOS), ensuring high intensity of the map as well as a relatively large energy distance between the two points in order to exclude potential overlaps of experimental energy windows (see supplementary information). Orbitals with p_z character, in our definition parallel to the $[001]$ zone axis and parallel to the electron beam, have little influence on the p_x and p_y orbital maps due to their symmetry for this particular geometry and will not be mapped individually.

Compared to the O K-edge, the Ti $L_{2,3}$ -edge is harder to interpret and has more possible final wave functions. However, many of the cases can be disregarded for various reasons. Due to the chosen crystallographic direction of $[001]$, final orbitals with d_{z^2} character can be excluded for symmetry reasons similar to the p_z orbitals before. $d_{x^2-y^2}$ and d_{xy} exhibit a four-lobed shape in the projection only for a one unit cell thick sample but lose any resemblance to a d-orbital for samples only a few nm thick (see Fig. S5 in the SI). Further, the general structure of the Ti DOS above Fermi level makes it hard to single out transitions to the $d_{x^2-y^2}$ or d_{xy} orbitals, which would result in orbital maps with either a strong contribution of other final states or an unfeasibly low signal-to-noise ratio. Thus, only d_{xz} and d_{yz} remain, both with dumbbell shapes resembling p orbitals for this specific projection. The orbital at an energy loss of 458.7 eV, projection oriented towards the closest O atoms, is defined as d_{xz} , while the orbital at 462.4 eV with a perpendicular projected orientation is defined as d_{yz} in this work.

Table 1: Parameters of the simulated reference images.

parameters	rutile	graphite	STO-LMO
thickness (1 unit cell) [\AA]	3	4.3	7.8
pixel size x [\AA]	0.14	0.15	0.36
pixel size y [\AA]	0.14	0.21	0.24
acceleration voltage [kV]	300	60	300
STEM convergence semi-angle α [mrad]	30	30	30
STEM collection semi-angle β [mrad]	50	50	50

3.1.1. STEM

In the following, we present the simulated STEM spectral images of the four cases discussed in the previous section. We focus on the influence of sample thickness, incident electron dose and convergence (collection) semi-angle α (β) on the image quality, i.e. the recognizability of the original projected orbital shapes.

The two upper rows in Fig. 1 show the two relevant cases of the O-K edge. They exhibit a drastically different sample thickness dependence, due to the preferred inelastic scattering direction parallel to the orbital orientation. In the case of the p_x orbital, when the sample thickness is increased, the perfect orbital shape deteriorates in the image due to the channeling effect [18, 31, 32] and due to partial waves created at neighbouring atomic columns in the bulk sample where the incident beam is already less focused. Thus, with increasing sample thickness, increasingly more intensity from the orbital shape is transferred to the closest Ti atom in the image, with the result that the two p_x lobes appear as a single, long ellipse. The channeling effect is significantly less pronounced for the p_y orbital due to the preferred scattering direction in between the (distorted) octahedra of the rutile crystal structure. Even for a projected sample thickness of 20 nm, the only perceivable change in the spectral image is a slight background intensity increase between the atoms. The dumbbell shape is mostly preserved. This is reflected in the comparatively low image difference indicated by the SIFT algorithm.

The third row in Fig. 1 shows the transitions to final states with d_{xz} character of the Ti-L₃ edge. Transitions to d_{yz} states are not explicitly shown, as they are basically equivalent to Fig. 1(g)-(i) except for the 90° rotation of the orbital shapes. Unlike for the O orbitals, here, the comparatively heavy Ti atom is at the center of the orbitals. This leads to

a focusing effect of the scattered electrons and with increasing thickness, the dumbbell shape shifts to a concentrated ellipse. We want to stress at this point that this is not a shortcoming that can be overcome by technical improvements of, e.g., the spatial/spectral resolution or the spot size of the electron beam, but solely by reducing the sample thickness, sometimes to unrealistic sizes. Nevertheless, while for this energy, the dumbbell shape is lost, the directional dependence is preserved for any thickness, thus the two relevant cases with final orbital d_{xz} and d_{xy} can still be distinguished.

The last row of Fig. 1 shows in detail the thickness dependence of the image difference of the O and Ti energy-filtered STEM images. For an acceleration voltage of 300 kV, all energy losses display a drastic difference increase in the first few nm followed by an only slight increase over the next tens of nm. However, for a voltage of 80 kV, the difference to the 300 kV reference image either fluctuates around 0.3 or increases only slightly with sample thickness. Interestingly enough, for nearly all cases, the choice of acceleration voltage and sample thickness (above 5 nm) seems to have little to no influence on the quality of the resulting orbital map. The only exception is the O p_y orbital for an acceleration voltage of 300 kV, displaying a considerably lower image difference compared to the other cases due to the aforementioned reasons.

While the simulated thickness scans as in Fig. 1 for an infinite electron dose are very useful for indicating general trends of the orbital maps in regards to the sample thickness, a more holistic view is gained when shot noise and the resulting signal-to-noise ratio is considered. We effectively simulate a certain electron incident dose by keeping a constant ratio between the electron counts in the image and the thickness dependent signal intensity. Thus, without knowing the relation between the absolute electron incident dose and the resulting image dose

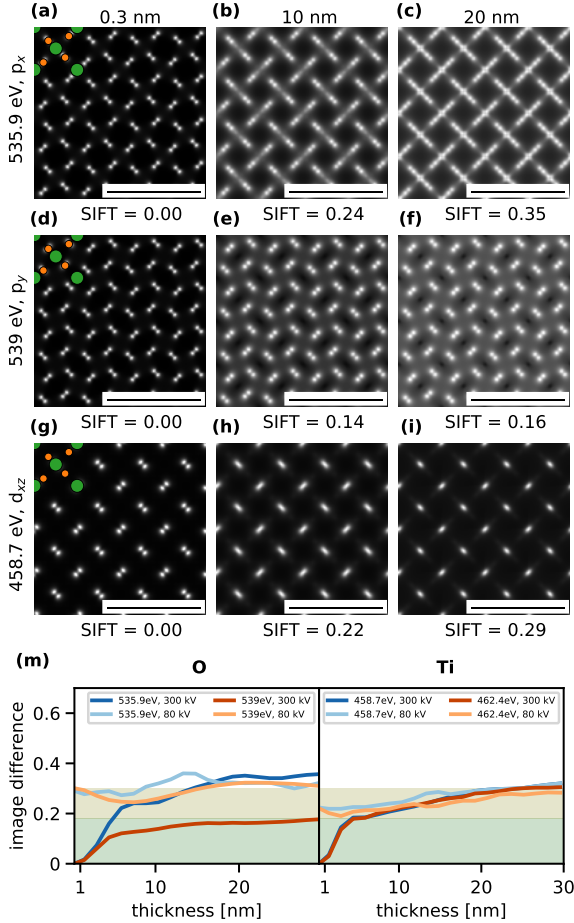


Figure 1: (a) - (i) Simulated STEM spectrum images of rutile in the $[001]$ zone axis for the indicated sample thickness and energy loss. All scale bars indicate 1 nm. Green and orange dots mark the positions of Ti and O atoms, respectively. (m) SIFT image difference as function of sample thickness. All image differences are relative to the respective energy loss spectral image for 0.3 nm sample thickness and 300 kV acceleration voltage.

in a given microscope, we can still give the relative incident dose and calculate the specific electron counts from a given reference case. We choose for the reference image dose $10^6 \text{ e}^-/\text{nm}^2$ for the 14.8 nm thick sample, as this should result in a representative range of image doses. A broad range of relative incident doses over several magnitudes is investigated. The image doses range from a few electrons for the whole image to many thousands, effectively approaching an infinite dose image. The resulting noisy images of the p_x orbitals are shown in Fig. 2.

In order to be able to properly gauge the effect the diminished signal-to-noise ratio has on the image quality, we again apply the image difference metric and use for each energy loss the respective infinite dose reference image with parameters according to Table 2. However, as all images are normalised for the comparison, changes in the total image intensity are not factored into the image difference. The results for the previously discussed four relevant energy losses are presented in Fig. 3. All cases exhibit the same general behaviour. Basically independent of sample thickness, an incident dose not lower than 1 % of the reference incident dose is required for the orbitals to be distinguishable from the noise. Contrary to the previous cases with infinite electron dose, the minimum for a given incident electron dose is no longer found at the thickness of a single unit cell. For very low doses, the minimum actually is at the thickest investigated sample, although we conjecture that the image difference would still drop for a higher sample thickness. For very high doses, on the other hand, an actual minimum is found at about 2 nm thickness, converging toward the value for an infinite electron dose.

The map of O p_y orbital (539 eV) shows a slightly different thickness dependence than the other cases, in agreement with the findings from Fig. 1. Above a thickness of about 5 nm, the image difference stays at a relatively low level and increases only negligibly with increasing thickness. This behaviour makes it the preferred case for experimental orbital mapping as long as high enough electron incident rates can be achieved without damaging the sample. Finally, for rutile STEM, we investigate the influence of the electron beam convergence semi-angle α on the quality of the orbital maps (Fig. 4). For a single unit cell thick sample, we find that a higher convergence angle always results in a qualitatively better orbital map. This result is not surprising for simulations without aberrations. As such, we have chosen

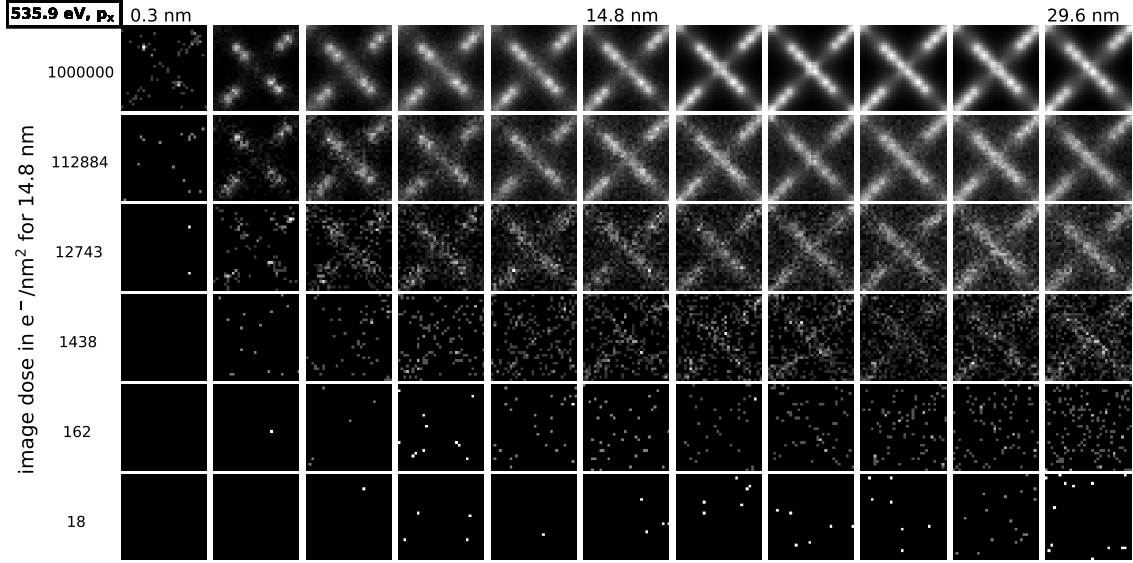


Figure 2: Simulated STEM spectrum images of a single rutile unit cell with added shot noise for varying sample thickness. The image dose values, chosen equidistant on a logarithmic scale, are given for the 14.8 nm thick sample. For the other cases, the image dose is scaled with the norm of the specific infinite dose image in order to simulate a constant incident dose. Shot noise is applied to a 4×4 unit cell image but only a single unit cell is shown. The images are individually normalized to the respective image intensity for better clarity.

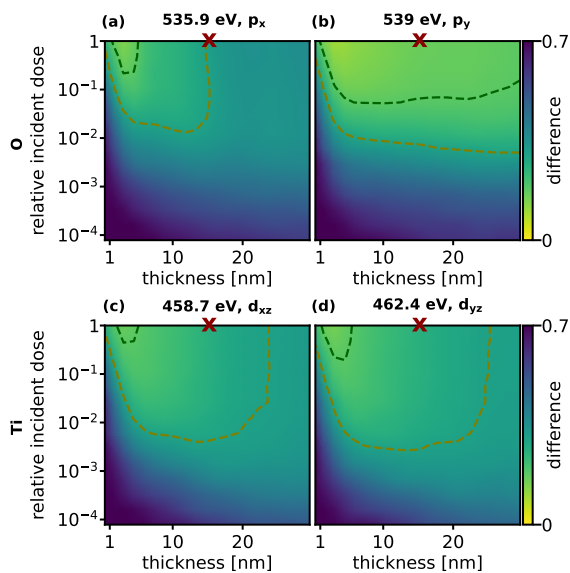


Figure 3: Image difference maps of STEM spectrum images of rutile. The incident dose is measured relative to the image dose of $10^6 \text{ e}^-/\text{nm}^2$ for the image belonging to a 14.8 nm thick sample, marked by the red x. The reference image in all cases is calculated with infinite incident electron dose. The dark green and the olive contour lines indicate an image difference of 0.18 and 0.3, respectively.

the spectral images for the highest investigated α as our reference images. It appears, however, that for increasing sample thickness, the α dependence of the difference almost completely disappears. Only for the smallest convergence semi-angle of 10 mrad a (marginally) higher image difference can be observed. We can conclude from this data that for realistic sample thicknesses, the choice of convergence semi-angle has little influence on the final orbital map. When, in addition, various collection semi-angles β are considered, it becomes apparent that, with few exceptions, $\beta < \alpha$ leads to higher image differences. Further, with $\beta > \alpha$ the change of image difference with increasing β is negligible. Considering, however, that an increase of β leads to a higher signal intensity and, thus, better signal-to-noise ratio, a larger β is advantageous in general, as long as large angle scattering effects like thermal diffuse scattering do not contribute to the signal.

3.1.2. TEM

In the following, we present the simulated energy-filtered TEM (EFTEM) images for the four energy losses already discussed previously. For simulation parameters where comparison to STEM is possible, such as sample thickness and incident electron dose,

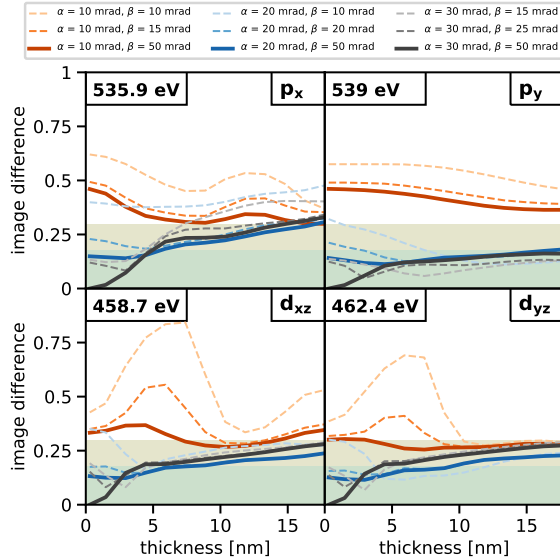


Figure 4: Rutile SIFT image difference as a function of sample thickness for an acceleration voltage of 300 kV and several convergence and collection semi-angles α and β . All image differences are relative to the orbital map for $\alpha = 30$ mrad and $\beta = 50$ mrad.

we will proceed fully analogously as in the previous section and compare the methods from a theoretical point of view. Instead of convergence angles, however, we will focus on the effect of (a small) defocus on the quality of the EFTEM orbital map. The upper two rows in Fig. 5 show very similar thickness dependence of the O EFTEM maps compared to the STEM spectrum images. However, for both energy losses, the degradation of the orbital shape due to elastic channeling seems even less pronounced. Nevertheless, the transition to the p_y orbital, situated at 539 eV energy loss, still appears to be the most favourable of the four discussed transitions for orbital mapping. While the O orbitals display less elastic channeling compared to STEM, the Ti orbitals display the opposite behaviour. Both cases show a strong transfer of intensity from the orbital to the O atoms, fluctuating with the sample thickness according to the Pendellösung. Further, it appears that the specific orientation of the orbital does not influence the amount of elastic channeling that occurs.

The thickness dependent image difference further highlights the difference in thickness dependence between EFTEM [Fig. 5(m)] and STEM [Fig. 1(m)] images. Firstly, with the exception of the O p_y

orbital, image differences are generally higher for EFTEM. At a thickness of one unit cell, however, the difference between 80 kV and 300 kV acceleration voltage are almost non-existent for EFTEM (under ideal conditions), in line with the reciprocity theorem [33, 34]. Secondly, the image difference fluctuates with sample thickness, especially noticeable for the Ti orbitals. While for STEM, a higher sample thickness generally means a higher image difference, this is not the case for EFTEM. On the contrary, in multiple cases, the image quality actually improves with thickness in some regions due to Pendellösung effects. This shows that finding the optimal sample thickness for EFTEM orbital mapping is entirely dependent on the particular energy loss, acceleration voltage, sample, and orientation.

Similar to the previous section, the dose dependent image difference maps (Fig. 6) further support the findings from the images with infinite electron dose. In general, the image difference maps for EFTEM are very similar to the STEM image difference maps (Fig. 3). Notable exceptions are the even less pronounced thickness dependent changes for O p_y images and the image difference fluctuations with sample thickness for Ti d_{xz} and d_{yz} .

Finally, we investigate the influence of defocus on the EFTEM maps for the largest rutile sample thickness investigated in this work, i.e., a sample 100 unit cells thick, corresponding to 29.6 nm (Fig. 7). We use the following sign convention: a negative defocus shifts the objective focus point from the bottom of the sample higher, i.e., inside the sample. For 80 kV, it becomes apparent that the image difference introduced by the sample thickness is too large for the defocus to be able to positively influence it to an acceptable range, with the singular exception of -3 nm defocus for the p_y orbital. Further, no clear trend can be discerned concerning the influence a defocus has on the image difference. For 300 kV, however, a clear trend is visible. A slightly negative defocus actually improves the similarity between the EFTEM image and the reference image, with the image difference minimum between -3 nm and -5 nm for all investigated energy losses. A positive defocus, however, has the opposite influence and very quickly (> 2 nm) worsens the energy-filtered image to the point of unrecognizability of any orbitals.

3.2. Graphite

For our second material, we have chosen graphite, as it consists entirely of light elements, in con-

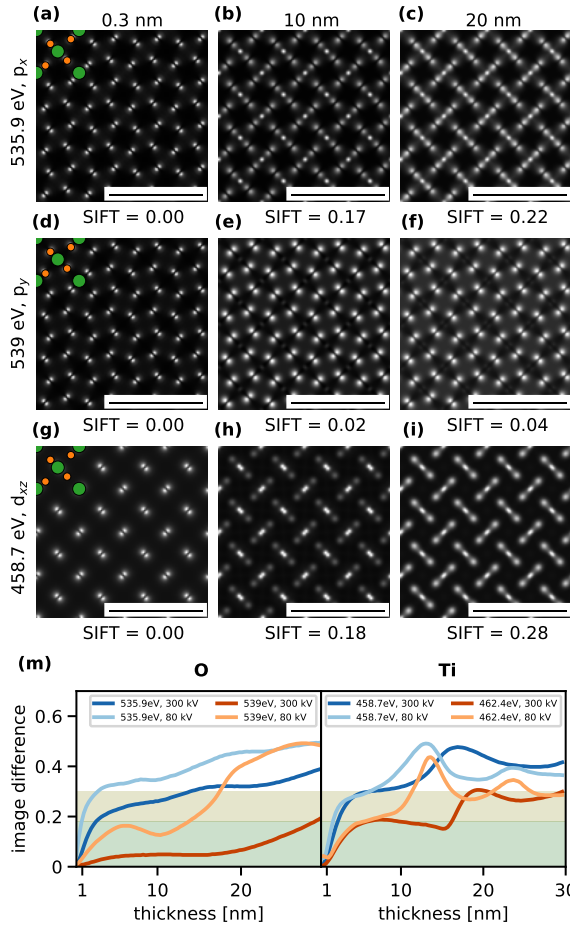


Figure 5: (a) - (l) Simulated energy-filtered TEM images of rutile in the [001] zone axis for the indicated sample thickness and energy loss. All scale bars indicate 1 nm. Green and orange dots mark the positions of Ti and O atoms, respectively. (m) SIFT image difference as function of sample thickness. All image differences are relative to the respective energy-filtered image for 0.3 nm sample thickness and 300 kV acceleration voltage.

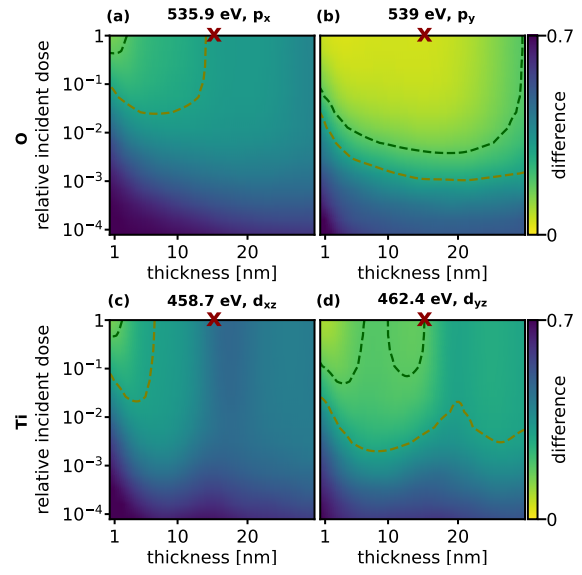


Figure 6: Image difference maps of EFTEM images of rutile. The incident dose is measured relative to the image dose of $10^6 e^-/\text{nm}^2$ for the image belonging to a 14.8 nm thick sample, marked by the red x. The reference image in all cases is calculated with infinite incident electron dose. The dark green and the olive contour lines indicate an image difference of 0.18 and 0.3, respectively.

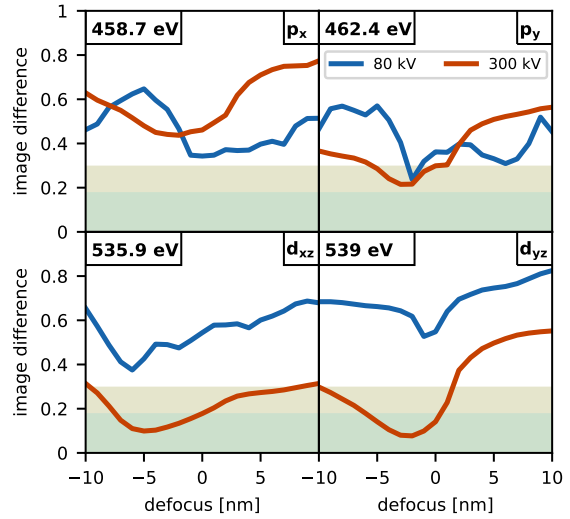


Figure 7: SIFT image difference of EFTEM images as a function of defocus for acceleration voltages of 80 kV and 300 kV and a sample thickness of 29.6 nm. All image differences are relative to the orbital map for 0 defocus.

trast to the material of the previous section, rutile. Graphite, especially its two-dimensional single layer form graphene, has received considerable attention in the last ~ 20 years [35, 36, 37], in particular, but not exclusively, due to its potential manifold applications in electronics.

Graphite consists of carbon layers in a hexagonal structure weakly bound by van der Waals forces. The high rotational symmetry of the individual graphene layers dictates the crystallographic direction necessary for orbital mapping. Conventionally, for graphene and similar two-dimensional materials, a top-down view is employed. In our case, however, this direction would result only in rotationally symmetric maps with negligible differences between different energy loss windows for pristine graphite [9, 38]. Thus, a side view is required and we opt to choose the $[1\ 0\ \bar{1}\ 0]$ zone axis, the same as in [10]. Two peaks dominate the DOS above the Fermi energy and, likewise, the energy loss near edge structure (ELNES) of the graphite K-edge. The first peak is a result of the π^* orbital, having mainly p_z angular momentum character. The second peak is a result of the σ^* orbital with a mixture of p_x , p_y and s atomic orbitals that combine to a sp^2 orbital. We simulate energy-filtered maps at 285.6 eV and 292.5 eV energy loss for the π^* and the σ^* orbitals, respectively. Contrary to the previous case of rutile, here, the slow changing DOS would allow for relatively large energy windows where the resulting orbital maps are basically the same. For graphite, we only consider a high tension of 60 kV as a higher acceleration voltage would already induce significant knock-on damage in the sample. [39]

3.2.1. STEM

The resulting STEM spectrum images are shown in Fig. 8. In the upper row, spectrum images for an energy loss of 285.6 eV are displayed. For a single unit cell thick sample, the characteristic dumbbell shape of the p_z orbitals is clearly visible. However, even for this thinnest possible sample, there is a small local intensity maximum at the positions of the C atoms due to the elastic scattering caused by the atomic columns. This effect is more pronounced with increasing sample thickness, resulting in the complete deterioration of the imaged dumbbell shapes to smeared out ellipses. As the sample thickness onset for this reshaping is already at thicknesses smaller than 5 nm, in practice, there is effectively no way to prevent it experimentally. Nevertheless, due to the channeling effect also being

present in the reference image, the resulting image differences are relatively small. The electron dose dependent image difference map in Fig. 8(g) further confirms this finding.

A similar trend can be observed for the spectrum images for an energy loss of 292.5 eV. Due to the projection, the σ^* orbitals appear as circular shapes significantly more confined to the atomic rows compared to the π^* orbitals. Horizontally, however, the intensity maxima are localized between the carbon positions. Thus, the elastic channeling effect of a thicker sample results primarily in a horizontal blurring and a comparatively low image difference to the reference image. In the dose-thickness difference map [Fig. 8(h)], a similar trend to Fig. 8(g), albeit more pronounced, can be observed. There is only little further increase of the image difference above 7 nm for all electron doses above 1 % relative dose. In contrast to the difference map of the π^* orbital, however, for medium to high electron doses, the image difference converges to the low value of 0.1.

In general, the graphite spectrum images appear to be a little bit more robust concerning thickness variations compared to the rutile spectrum images of the previous section. Possible explanations for this robustness are the low high tension of 60 kV (the reference image itself appears already less detailed) and that carbon is the only element in the unit cell (less chance for noticeable dechanneling). For changes in the electron beam convergence semi-angle α , however, there are significant differences to before. In the case of rutile, we arrived at the more or less general conclusion that for realistic sample thicknesses, the convergence angle played no significant role at all. For the π^* orbital of graphite, however, the choice of α is crucial [Fig. 9(a)]. The larger beam crossover for $\alpha = 20$ mrad results in the loss of the ability to resolve the individual dumbbells in the image. Further, $\alpha = 10$ mrad results in an effect similar to a contrast inversion. The beam crossover is large enough that the probe can excite inelastic transitions in two layers when the beam is centered between layers. Centered on the atomic layers, however, only transitions in the respective layer can be triggered, resulting in less intensity in the STEM-EELS map and a contrast inversion. For a sample thickness between 9 nm and 15 nm, however, we theorize that channeling effects again reverse this effect. The result is a large decrease in image difference for this thickness range. The thickness and α dependent STEM-EELS maps can

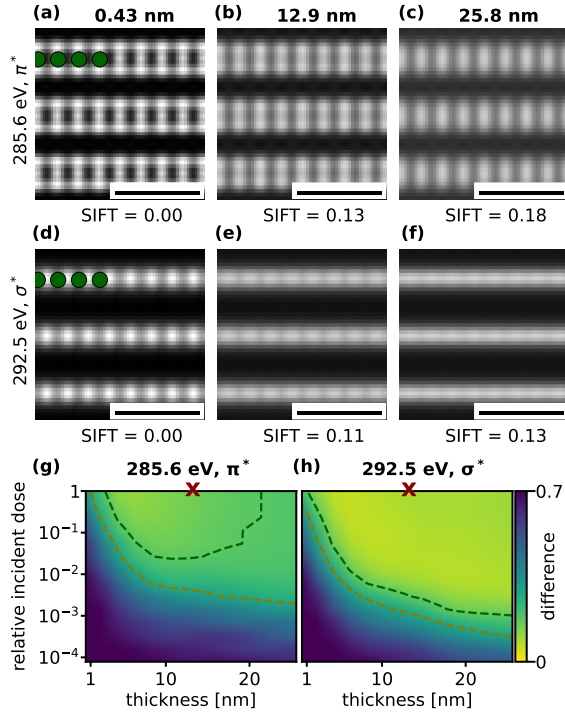


Figure 8: (a) - (f) Simulated STEM spectrum images of graphite in the $[10\bar{1}0]$ zone axis for the indicated sample thickness and energy loss with an infinite electron dose. All scale bars indicate 0.5 nm. Green dots mark the positions of C atoms. (g), (h) Image difference maps of the graphite spectrum images for the indicated energy losses. The incident dose is measured relative to the image dose of 10^6 e^-/nm^2 for the image of a 12.8 nm thick sample, marked by the red x. The reference image in all cases is calculated with infinite electron dose. The dark green and olive contour lines indicate an image difference of 0.18 and 0.3, respectively.

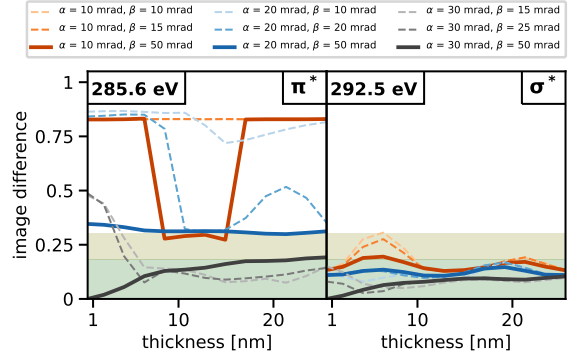


Figure 9: Graphite SIFT image difference as a function of sample thickness for an acceleration voltage of 60 kV and several convergence and collection semi-angles α and β . All image differences are relative to the orbital map for $\alpha = 30$ mrad and $\beta = 50$ mrad.

be seen in Fig. S13 in the supplementary information. In the case of the σ^* orbital, however, the convergence angle again has very little influence on the quality of the orbital map [Fig. 9(b)].

3.2.2. TEM

In the following, we present the EFTEM orbital maps of the graphite π^* and σ^* orbitals simulated with parameters corresponding to those of the STEM spectrum images in the previous subsection. While the basic shape of the orbitals in the reference images for a one unit cell thick sample is in principle the same as in the STEM images, there are some distinctions that influence the SIFT image differences. The orbitals in EFTEM for both energy losses appear more sharply and with clearer edges. Further, for the π^* orbitals, there is no intensity at all directly at the positions of the carbon atoms, the two lobes of the p orbital are distinctly separated. This was also the case for all investigated sample thicknesses. Further, an increase in sample thickness results in a large intensity increase between the atomic columns. This effect continues up to the point where the background intensity is nearly as high as the intensity of the orbitals themselves. For finite incident electron dose, this effect is especially pronounced with the result of a very large image difference. The image difference map in Fig. 10(g) shows a steep jump in image difference around 14 nm, from which thickness on the features of the orbitals are no longer discernible from the background.

For the σ^* orbital the preferred inelastic scattering

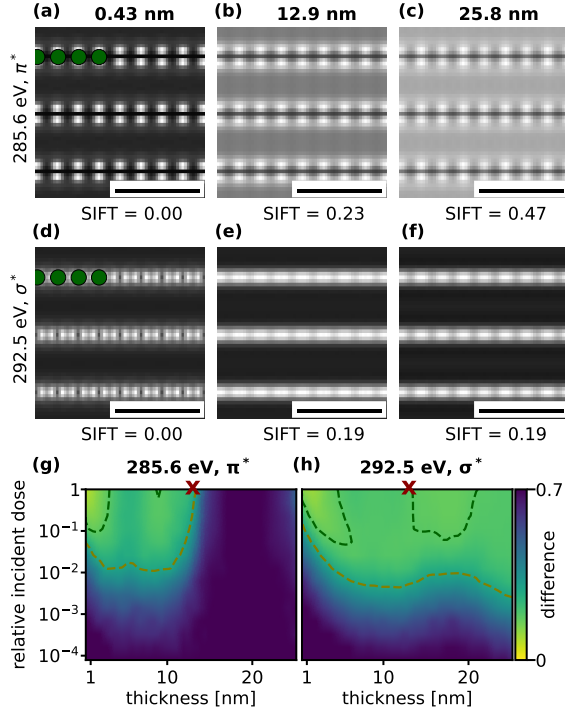


Figure 10: Exactly the same as Fig. 8 but with simulated EFTEM images.

direction is mainly in the plane of the carbon sheets, leading to the opposite result compared to the π^* case. The circular shapes at the positions of the carbon atoms are fully smeared out in the horizontal direction for samples exceeding 5 nm. We want to emphasize here that this effect is a fundamental result of the electron propagation through the material, i.e., it cannot be overcome with an increase in spatial or spectral resolution, only with a thinner sample. The thickness – dose difference map, however, reveals an oscillatory thickness dependence, similar to the rutile EFTEM images. Due to this oscillation, a sample thickness between 18 nm and 22 nm again nearly allows to distinguish individual orbitals. As for rutile, we have investigated the dependence of the image difference on the defocus (Fig. 11). For the energy loss of 285.6 eV, no image improvement is achieved by either under- or overfocusing. On the contrary, for relatively thick samples of 25.6 nm, already a small defocus of 1 nm in either direction is detrimental for the orbital image. This again highlights the tremendous precision required for orbital mapping. For the energy loss of 292.5 eV, we see, similar to the rutile EFTEM

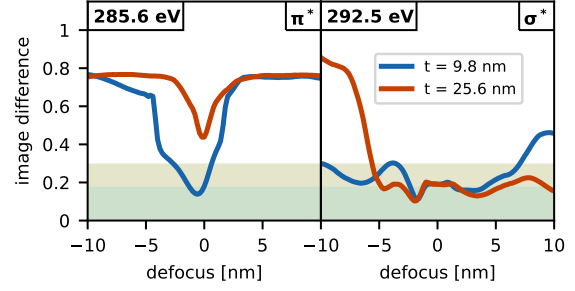


Figure 11: SIFT image difference of EFTEM images as a function of defocus for graphite sample thicknesses of 9.8 nm and 25.6 nm. All image differences are relative to the orbital map for 0 defocus.

images, a significant improvement of image quality for a small (between -5 and -2 nm) defocus. In this case, however, the sample thickness has little influence on the effect of the defocus on the image.

3.3. STO-LMO

The last structure of our parameter investigation is a heterostructure consisting of the two perovskites SrTiO_3 (STO) and LaMnO_3 (LMO). Perovskites are a structure model of ever more increasing public interest [40, 41] due to their extreme range in synthesizable properties like superconductivity, ferroelectricity and ferromagnetism [42]. The combination of thin layers of different perovskites to a heterostructure allows the already widespread application of perovskites as lasers, LEDs, photodetectors and solar cells [43, 44, 45, 46, 47, 48]. The cubic perovskite STO has the space-group $Pm\bar{3}m$ with lattice parameter $a_{\text{STO}} = 3.905 \text{ \AA}$ [49]. In contrast, LMO displays rhombohedral symmetry according to the $R\bar{3}c$ space group with lattice parameters $a_{\text{LMO}} = 5.508 \text{ \AA}$ and $c_{\text{LMO}} = 13.310 \text{ \AA}$ [50]. While the structure is very similar to the cubic perovskite structure, the MnO_6 octahedra are rotated a few degrees relative to each other, reducing the crystal symmetry [51]. For epitaxial deposition on a STO substrate, however, LMO is formed in a pseudo-cubic perovskite structure with an effective lattice parameter $a_{\text{effLMO}} = 3.914 \text{ \AA}$ [52, 53]. Due to the almost perfect match between the structure parameters (0.2 % mismatch), a stable heterostructure can be constructed. Computational constraints limit us to a periodic structure of 4 unit cells of each of the materials. Both, a Ti–La terminated interface

and a Mn–Sr terminated interface are present in the structure (presented in supplementary information). However, we will exclusively focus on the Ti–La interface including the first adjacent unit cells, thus the supercell size is more than sufficient.

Due to the presence of oxygen in both perovskites, we have selected the O K-edge for orbital mapping. In particular, two energy losses are of interest for the [100] zone axis. At 533.4 eV, the imaged orbitals of the specific O atoms located between Sr atoms display an orientation perpendicular to the interface, which we will define as p_x orbitals in this work. The corresponding LMO O atoms located between La atoms, however, display an orthogonal direction, which we will define as p_y orbitals. These specific orbitals are of special interest as they, contrary to most of the remaining O orbitals, display a consistent orientation over all unit cells of the corresponding material and over energy windows as large as 1 eV (Fig. S4 in the SI). At the second chosen energy loss, however, at 536.7 eV, the orbitals swap their orientation with each other. The previous p_x orbitals of STO have changed to p_y orbitals and vice versa for LMO. Even though the mentioned orbitals are of particular interest to us, we will present EFTEM and STEM spectrum images of all the orbitals in close proximity to the Ti–La terminated interface. Likewise, the SIFT image difference will take into account all the orbitals.

3.3.1. STEM

The resulting STEM spectrum images are shown in Fig. 12. The upper row in Fig. 12 displays the result for an energy loss of 533.4 eV. There is a clear distinction between the two parts of the heterostructure. In the region of interest, marked by the red rectangle, the p-like orbitals are oriented perpendicular to each other. Another noticeable difference is that in the LMO region, all observed orbitals are blurry and less distinct. This is a direct consequence of the rotation of the MnO_6 octahedra. The slightly varying projected positions of the O atoms lead to an overlay of orbital images and, thus, less distinct shapes. Increasing the sample thickness results in a relative intensity increase at the positions of the heavier Ti and Mn atoms due to channeling effects. Further, at these positions, the originally p-like shapes deteriorate to a circularly symmetric shape. Thus, all potential extractable directional orbital information is lost. On the other hand, this relative intensity increase leads to an intensity decrease in our region of interest and the

STO p_x orbitals have nearly vanished for a sample thickness larger than 10 nm.

The situation is very similar for the energy loss of 536.7 eV. While the effects of channeling along Ti and Mn columns are just as present, there are a few differences. As mentioned before, most of the orbitals have switched their orientation, in particular all of the orbitals in the marked region. However, of the STO p_y orbitals, only the one closest to the interface is visible. Nevertheless, for both energy losses, the majority of details and orbital information vanishes for increasing sample thickness. The thickness–dose plots [Fig. 12(g) and (h)] further confirm this. Although the image difference appears to reach a plateau for all incident doses above 8–10 nm, the difference values are in both cases above the acceptable threshold and, in general, significantly higher than for the previous materials. Increasing or decreasing the electron beam convergence semi-angle α appears to have no significant influence on the orbital map quality for a sample thickness above 10 nm (Fig. 13). This is in line with the α dependence of STEM orbital maps for rutile (Fig. 4) and the σ^* orbital of graphite [Fig. 9(b)], although for STO–LMO, the effect is even more pronounced.

3.3.2. TEM

The EFTEM images for the STO–LMO heterostructure are presented in Fig. 14 and are remarkably similar to the STEM spectrum images presented in the previous section. However, while an increasing sample thickness still shows a relative intensity shift to the Ti and Mn sites, it is less severe than in the STEM case. The resulting image difference numbers are relatively low, even for realistically thick samples. The thickness–dose plots [Fig. 14(g) and (h)] show acceptable differences up to 17 nm for 533.4 eV and up to 20 nm for 536.7 eV, as long as a high enough electron dose is used. In the latter case, the effect of the Pendellösung can be clearly observed, in the same way as for the rutile and graphite EFTEM images before. There is a periodicity in the image difference dependent on the sample thickness which leads to an "island" of low image difference from 11 nm to 13 nm. Taking these effects into account, it seems that for this particular structure, EFTEM is more suited to the task from a purely image forming point of view. A small defocus of -1 nm to -3 nm can further improve the image quality, following the same apparent pattern as the other investigated materials

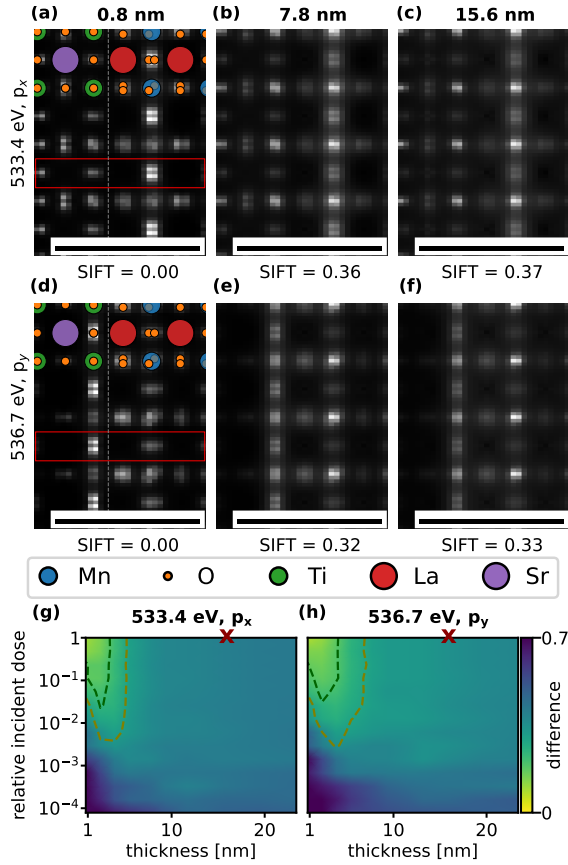


Figure 12: (a) – (f) Simulated STEM spectrum images of the interface between STO and LMO in the $[100]$ zone axis for both materials, the indicated sample thickness and energy loss with an infinite electron dose. All scale bars indicate 1 nm. (g), (h) Image difference maps of the STO-LMO spectrum images for the indicated energy losses. The incident dose is measured relative to the image dose of $10^6 \text{ e}^-/\text{nm}^2$ for the image of a 15.6 nm thick sample, marked by the red x. The reference image in all cases is calculated with infinite electron dose. The dark green and olive contour lines indicate an image difference of 0.18 and 0.3, respectively.

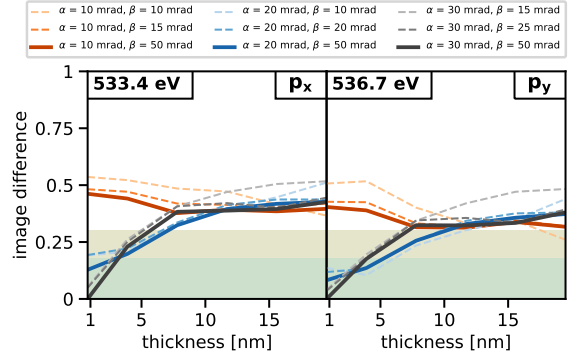


Figure 13: STO-LMO SIFT image difference as a function of sample thickness for an acceleration voltage of 300 kV and several convergence and collection semi-angles α and β . All image differences are relative to the orbital map for $\alpha = 30 \text{ mrad}$ and $\beta = 50 \text{ mrad}$.

but with less ambivalence in this case (Fig. 15).

4. Discussion and Conclusion

In this work, we have successfully applied an image difference metric to energy-filtered (S)TEM images with the goal of identifying optimal sets of parameters for imaging. The specific materials, i.e., rutile, graphite and a heterostructure of SrTiO_3 - LaMnO_3 , and the energy windows have been selected such that underlying electronic transitions can be mapped in real space. Thus, in principle, these orbital maps allow to directly measure the spatial dependence of initially unoccupied orbitals above Fermi energy. We have accomplished the task of finding suitable sets of parameters by calculating and minimizing the image difference between a perfect, albeit unachievable, image and the image for the specific set of parameters.

In the process of finding the optimal, or at least acceptable, sample thickness of the chosen materials, we have encountered a fundamental inequality between EFTEM images and STEM spectral images concerning the dependence of the image difference on sample thickness. While the image difference of the STEM orbital maps increases fairly monotonically with the thickness, the EFTEM orbital maps display a periodicity which leads in many cases to comparably thicker samples being still acceptable. Further, in almost all the investigated cases, a slight defocus of -2 nm to -5 nm further decreased the EFTEM image difference. It appears that, in principle, EFTEM has the advantage over STEM

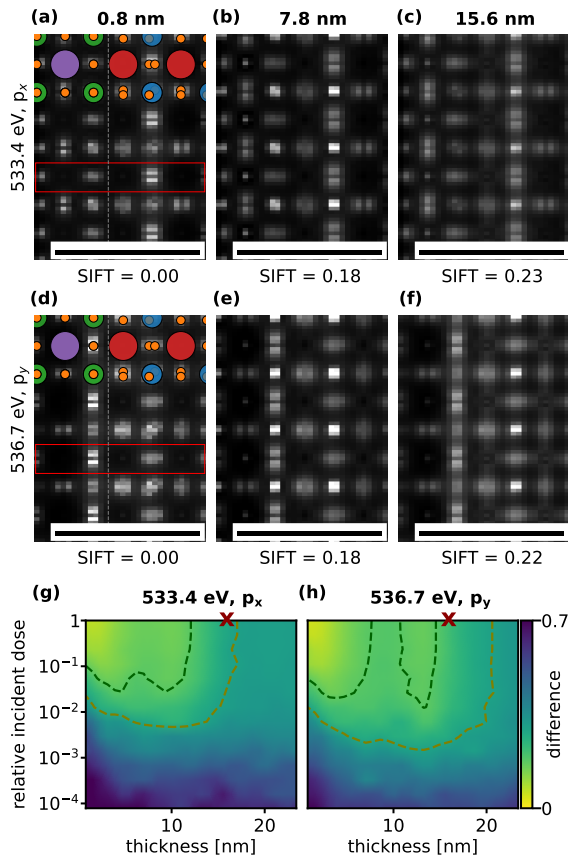


Figure 14: The same as in Fig. 12 but with simulated EFTEM images.

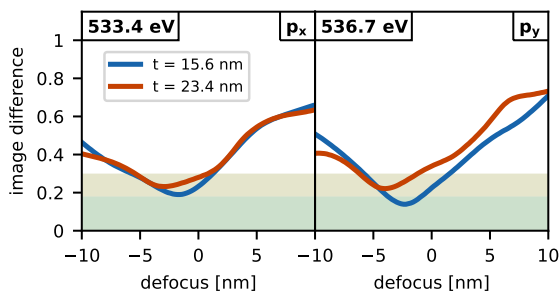


Figure 15: SIFT image difference of EFTEM images as a function of defocus for an STO-LMO interface with sample thicknesses of 15.6 nm and 23.4 nm. All image differences are relative to the orbital map for 0 defocus.

concerning the difficulty and strictness in sample preparation. However, this can only be certainly said for the assumed ideal imaging conditions, i.e. no aberrations or other lens errors, no sample drift or damage and no noise beside shot noise. Under more realistic conditions the preference could easily shift towards STEM, as it is in general easier for STEM to apply post-processing in order to mitigate non-ideal imaging conditions. Otherwise, we do not find a fundamental preference for either EFTEM or STEM in regards of orbital mapping.

In conclusion, orbital mapping, although not universally applicable (yet), proves to be a valuable tool when employed with meticulous planning and extensive theoretical simulations. For each of the materials investigated, we find certain parameter ranges together with a realistically achievable sample thickness that result in images with distinctly recognizable orbital shapes. Even when a finite electron dose and shot noise is considered, orbital mapping promises to provide valuable insights into the electronic structure and chemical binding of specific materials.

We acknowledge financial support by the Austrian Science Fund (FWF) under grant number I4309-N36. Further, we acknowledge TU Wien Bibliothek for financial support through its Open Access Funding Programme. The computational results presented were achieved, in part, using the Vienna Scientific Cluster (VSC).

References

- [1] D. J. Smith, Progress and perspectives for atomic-resolution electron microscopy, *Materials Today* 12 (2010) 10–16. doi:[https://doi.org/10.1016/S1369-7021\(10\)70140-1](https://doi.org/10.1016/S1369-7021(10)70140-1). URL <https://www.sciencedirect.com/science/article/pii/S1369702110701401>
- [2] M. Varela, M. P. Oxley, W. Luo, J. Tao, M. Watanabe, A. R. Lupini, S. T. Pantelides, S. J. Pennycook, Atomic-resolution imaging of oxidation states in manganites, *Phys. Rev. B* 79 (2009) 085117. doi:10.1103/PhysRevB.79.085117. URL <https://link.aps.org/doi/10.1103/PhysRevB.79.085117>
- [3] S. Lazar, Y. Shao, L. Gunawan, R. Nechache, A. Pignolet, G. A. Botton, Imaging, core-loss, and low-loss electron-energy-loss spectroscopy mapping in aberration-corrected stem, *Microscopy and Microanalysis* 16 (4) (2010) 416–424. doi:10.1017/S1431927610013504.
- [4] M. Bosman, V. J. Keast, J. L. García-Muñoz, A. J. D’Alfonso, S. D. Findlay, L. J. Allen, Two-dimensional mapping of chemical information at

- atomic resolution, *Phys. Rev. Lett.* 99 (2007) 086102. doi:10.1103/PhysRevLett.99.086102.
URL <https://link.aps.org/doi/10.1103/PhysRevLett.99.086102>
- [5] G. Kothleitner, M. J. Neish, N. R. Lugg, S. D. Findlay, W. Grogger, F. Hofer, L. J. Allen, Quantitative elemental mapping at atomic resolution using x-ray spectroscopy, *Phys. Rev. Lett.* 112 (2014) 085501. doi:10.1103/PhysRevLett.112.085501.
URL <https://link.aps.org/doi/10.1103/PhysRevLett.112.085501>
- [6] L. J. Allen, A. J. D'Alfonso, B. Freitag, D. O. Klenov, Chemical mapping at atomic resolution using energy-dispersive x-ray spectroscopy, *MRS Bulletin* 37 (2012) 47–52. doi:10.1557/mrs.2011.331.
URL <https://doi.org/10.1557/mrs.2011.331>
- [7] M.-W. Chu, S. C. Liou, C.-P. Chang, F.-S. Choa, C. H. Chen, Emergent chemical mapping at atomic-column resolution by energy-dispersive x-ray spectroscopy in an aberration-corrected electron microscope, *Phys. Rev. Lett.* 104 (2010) 196101. doi:10.1103/PhysRevLett.104.196101.
URL <https://link.aps.org/doi/10.1103/PhysRevLett.104.196101>
- [8] S. Löffler, M. Bugnet, N. Gauquelin, S. Lazar, E. Assmann, K. Held, G. A. Botton, P. Schattschneider, Real-space mapping of electronic orbitals, *Ultramicroscopy* 177 (2017) 26 – 29. doi:https://doi.org/10.1016/j.ultramic.2017.01.018.
URL <http://www.sciencedirect.com/science/article/pii/S0304399117300517>
- [9] L. Pardini, S. Löffler, G. Biddau, R. Hambach, U. Kaiser, C. Draxl, P. Schattschneider, Mapping atomic orbitals with the transmission electron microscope: Images of defective graphene predicted from first-principles theory, *Phys. Rev. Lett.* 117 (2016) 036801. doi:10.1103/PhysRevLett.117.036801.
URL <https://link.aps.org/doi/10.1103/PhysRevLett.117.036801>
- [10] M. Bugnet, M. Ederer, V. K. Lazarov, L. Li, Q. M. Ramasse, S. Löffler, D. M. Kepaptsoglou, Imaging the spatial distribution of electronic states in graphene using electron energy-loss spectroscopy: Prospect of orbital mapping, *Phys. Rev. Lett.* 128 (2022) 116401. doi:10.1103/PhysRevLett.128.116401.
URL <https://link.aps.org/doi/10.1103/PhysRevLett.128.116401>
- [11] J. Repp, G. Meyer, S. Paavilainen, F. E. Olsson, M. Persson, Imaging bond formation between a gold atom and pentacene on an insulating surface, *Science* 312 (5777) (2006) 1196–1199. arXiv:https://www.science.org/doi/pdf/10.1126/science.1126073, doi:10.1126/science.1126073.
URL <https://www.science.org/doi/abs/10.1126/science.1126073>
- [12] L. Gross, F. Mohn, N. Moll, P. Liljeroth, G. Meyer, The chemical structure of a molecule resolved by atomic force microscopy, *Science* 325 (5944) (2009) 1110–1114. arXiv:https://www.science.org/doi/pdf/10.1126/science.1176210, doi:10.1126/science.1176210.
URL <https://www.science.org/doi/abs/10.1126/science.1176210>
- [13] E. I. Altman, M. Z. Baykara, U. D. Schwarz, Noncontact atomic force microscopy: An emerging tool for fundamental catalysis research, *Accounts of Chemical Research* 48 (9) (2015) 2640–2648, pMID: 26301490. arXiv:https://doi.org/10.1021/acs.accounts.5b00166, doi:10.1021/acs.accounts.5b00166.
URL <https://doi.org/10.1021/acs.accounts.5b00166>
- [14] D. Silverstein, J. Farrell, The relationship between image fidelity and image quality, in: *Proceedings of 3rd IEEE International Conference on Image Processing*, Vol. 1, 1996, pp. 881–884 vol.1. doi:10.1109/ICIP.1996.559640.
- [15] Zhou Wang, A. C. Bovik, H. R. Sheikh, E. P. Simoncelli, Image quality assessment: from error visibility to structural similarity, *IEEE Transactions on Image Processing* 13 (4) (2004) 600–612. doi:10.1109/TIP.2003.819861.
- [16] M. Pedersen, J. Hardeberg, Survey of full-reference image quality metrics, *Høgskolen i Gjøviks rapportserie* (06 2009).
- [17] S. Löffler, V. Motsch, P. Schattschneider, A pure state decomposition approach of the mixed dynamic form factor for mapping atomic orbitals, *Ultramicroscopy* 131 (2013) 39 – 45. doi:https://doi.org/10.1016/j.ultramic.2013.03.021.
URL <http://www.sciencedirect.com/science/article/pii/S0304399113000910>
- [18] E. J. Kirkland, *Advanced Computing in Electron Microscopy*, Springer, Boston, MA, 2010.
URL <https://link.springer.com/book/10.1007/978-1-4419-6533-2#toc>
- [19] J. M. Cowley, A. F. Moodie, The scattering of electrons by atoms and crystals. i. a new theoretical approach, *Acta Crystallographica* 10 (10) (1957) 609–619. doi:10.1107/S0365110X57002194.
URL <https://doi.org/10.1107/S0365110X57002194>
- [20] S. Löffler, Study of real space wave functions with electron energy loss spectrometry, Ph.D. thesis, Vienna University of Technology (2013).
- [21] P. Schattschneider, *Fundamentals of Inelastic Electron Scattering*, Springer, 1986.
URL [http://refhub.elsevier.com/S0304-3991\(17\)30051-7/sbref0032](http://refhub.elsevier.com/S0304-3991(17)30051-7/sbref0032)
- [22] P. Blaha, K. Schwarz, F. Tran, R. Laskowski, G. K. H. Madsen, L. D. Marks, Wien2k: An apw+lo program for calculating the properties of solids, *The Journal of Chemical Physics* 152 (7) (2020) 074101. arXiv:https://doi.org/10.1063/1.5143061, doi:10.1063/1.5143061.
URL <https://doi.org/10.1063/1.5143061>
- [23] M. Ederer, S. Löffler, Image difference metrics for high-resolution electron microscopy, *Ultramicroscopy* 240 (2022) 113578. doi:https://doi.org/10.1016/j.ultramic.2022.113578.
URL <https://www.sciencedirect.com/science/article/pii/S0304399122001085>
- [24] D. G. Lowe, Object recognition from local scale-invariant features, in: *Proceedings of the Seventh IEEE International Conference on Computer Vision*, Vol. 2, 1999, pp. 1150–1157 vol.2. doi:10.1109/ICCV.1999.790410.
- [25] L. A. Grunes, R. D. Leapman, C. N. Wilker, R. Hoffmann, A. B. Kunz, Oxygen *k* near-edge fine structure: An electron-energy-loss investigation with comparisons to new theory for selected 3*d* transition-metal oxides, *Phys. Rev. B* 25 (1982) 7157–7173. doi:10.1103/PhysRevB.25.7157.

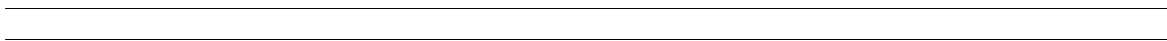
- URL <https://link.aps.org/doi/10.1103/PhysRevB.25.7157>
- [26] B. Jiang, J. M. Zuo, N. Jiang, M. O’Keeffe, J. C. H. Spence, Charge density and chemical bonding in rutile, TiO₂, *Acta Crystallographica Section A* 59 (4) (2003) 341–350. doi:10.1107/S010876730301122X. URL <https://doi.org/10.1107/S010876730301122X>
- [27] F. M. Hossain, L. Sheppard, J. Nowotny, G. E. Murch, Optical properties of anatase and rutile titanium dioxide: Ab initio calculations for pure and anion-doped material, *Journal of Physics and Chemistry of Solids* 69 (7) (2008) 1820–1828. doi:<https://doi.org/10.1016/j.jpccs.2008.01.017>. URL <https://www.sciencedirect.com/science/article/pii/S0022369708000413>
- [28] M. Landmann, E. Rauls, W. G. Schmidt, The electronic structure and optical response of rutile, anatase and brookite tio₂, *Journal of Physics: Condensed Matter* 24 (19) (2012) 195503. doi:10.1088/0953-8984/24/19/195503. URL <https://dx.doi.org/10.1088/0953-8984/24/19/195503>
- [29] M. Tinkham, *Group Theory and Quantum Mechanics*, Dover Books on Chemistry and Earth Sciences, Dover Publications, 2003. URL <https://books.google.at/books?id=r4GIU2wJCAEC>
- [30] M. Oberaigner, D. Knez, G. Kothleitner, S. Löffler, Post-processing paths for orbital mapping of rutile by stem-eels, in: *EUROMAT, 2021, european Congress and Exhibition on Advanced Materials and Processes*. URL <https://www.euromat2021.org/>
- [31] R. F. Loane, E. J. Kirkland, J. Silcox, Visibility of single heavy atoms on thin crystalline silicon in simulated annular dark-field STEM images, *Acta Crystallographica Section A* 44 (6) (1988) 912–927. doi:10.1107/S0108767388006403. URL <https://doi.org/10.1107/S0108767388006403>
- [32] P. Schattschneider, B. Jouffrey, Channeling, localization and the density matrix in inelastic electron scattering, *Ultramicroscopy* 96 (3) (2003) 453–462, proceedings of the International Workshop on Strategies and Advances in Atomic Level Spectroscopy and Analysis. doi:[https://doi.org/10.1016/S0304-3991\(03\)00107-4](https://doi.org/10.1016/S0304-3991(03)00107-4). URL <https://www.sciencedirect.com/science/article/pii/S0304399103001074>
- [33] M. von Laue, *Materiewellen und ihre Interferenzen*, Vol. 7, Akademische Verlagsgesellschaft Geest & Portig, 1948.
- [34] J. M. Cowley, Image Contrast in a Transmission Scanning Electron Microscope, *Applied Physics Letters* 15 (2) (1969) 58–59. arXiv:https://pubs.aip.org/aip/apl/article-pdf/15/2/58/7727861/58_1_online.pdf, doi:10.1063/1.1652901. URL <https://doi.org/10.1063/1.1652901>
- [35] M. I. Katsnelson, Graphene: carbon in two dimensions, *Materials Today* 10 (1) (2007) 20–27. doi:[https://doi.org/10.1016/S1369-7021\(06\)71788-6](https://doi.org/10.1016/S1369-7021(06)71788-6). URL <https://www.sciencedirect.com/science/article/pii/S1369702106717886>
- [36] A. K. Geim, K. S. Novoselov, The rise of graphene, *Nature Materials* 6 (3) (2007) 183–191. doi:10.1038/nmat1849. URL <https://doi.org/10.1038/nmat1849>
- [37] K. S. Novoselov, A. K. Geim, S. V. Morozov, D. Jiang, Y. Zhang, S. V. Dubonos, I. V. Grigorieva, A. A. Firsov, Electric field effect in atomically thin carbon films, *Science* 306 (5696) (2004) 666–669. arXiv:<https://www.science.org/doi/pdf/10.1126/science.1102896>, doi:10.1126/science.1102896. URL <https://www.science.org/doi/abs/10.1126/science.1102896>
- [38] A. H. Tavabi, P. Rosi, E. Rotunno, A. Roncaglia, L. Belsito, S. Frabboni, G. Pozzi, G. C. Gazzadi, P.-H. Lu, R. Nijland, M. Ghosh, P. Tiemeijer, E. Karimi, R. E. Dunin-Borkowski, V. Grillo, Experimental demonstration of an electrostatic orbital angular momentum sorter for electron beams, *Phys. Rev. Lett.* 126 (2021) 094802. doi:10.1103/PhysRevLett.126.094802. URL <https://link.aps.org/doi/10.1103/PhysRevLett.126.094802>
- [39] J. C. Meyer, F. Eder, S. Kurasch, V. Skakalova, J. Kotakoski, H. J. Park, S. Roth, A. Chuvilin, S. Eychen, G. Benner, A. V. Krashennnikov, U. Kaiser, Accurate measurement of electron beam induced displacement cross sections for single-layer graphene, *Phys. Rev. Lett.* 108 (2012) 196102. doi:10.1103/PhysRevLett.108.196102. URL <https://link.aps.org/doi/10.1103/PhysRevLett.108.196102>
- [40] A. Bhalla, R. Guo, R. Roy, The perovskite structure—a review of its role in ceramic science and technology, *Materials Research Innovations* 4 (1) (2000) 3–26. arXiv:<https://doi.org/10.1007/s100190000062>, doi:10.1007/s100190000062. URL <https://doi.org/10.1007/s100190000062>
- [41] M. Fiebig, Revival of the magnetoelectric effect, *Journal of Physics D: Applied Physics* 38 (8) (2005) R123. doi:10.1088/0022-3727/38/8/R01. URL <https://dx.doi.org/10.1088/0022-3727/38/8/R01>
- [42] H. Liu, X. Yang, A brief review on perovskite multiferroics, *Ferroelectrics* 507 (1) (2017) 69–85. arXiv:<https://doi.org/10.1080/00150193.2017.1283171>, doi:10.1080/00150193.2017.1283171. URL <https://doi.org/10.1080/00150193.2017.1283171>
- [43] X. Cheng, Y. Han, B.-B. Cui, Fabrication strategies and optoelectronic applications of perovskite heterostructures, *Advanced Optical Materials* 10 (5) (2022) 2102224. arXiv:<https://onlinelibrary.wiley.com/doi/pdf/10.1002/adom.202102224>, doi:<https://doi.org/10.1002/adom.202102224>. URL <https://onlinelibrary.wiley.com/doi/abs/10.1002/adom.202102224>
- [44] M. I. H. Ansari, A. Qurashi, M. K. Nazeeruddin, Frontiers, opportunities, and challenges in perovskite solar cells: A critical review, *Journal of Photochemistry and Photobiology C: Photochemistry Reviews* 35 (2018) 1–24. doi:<https://doi.org/10.1016/j.jphotochemrev.2017.11.002>. URL <https://www.sciencedirect.com/science/article/pii/S1389556717301144>
- [45] H. J. Snaith, Perovskites: The emergence of a new era for low-cost, high-efficiency solar cells, *The Journal of Physical Chemistry Letters* 4 (21) (2013) 3623–3630. arXiv:<https://doi.org/10.1021/jz4020162>, doi:10.1021/jz4020162. URL <https://doi.org/10.1021/jz4020162>

- [46] W.-J. Yin, T. Shi, Y. Yan, Unique properties of halide perovskites as possible origins of the superior solar cell performance, *Advanced Materials* 26 (27) (2014) 4653–4658. arXiv:<https://onlinelibrary.wiley.com/doi/pdf/10.1002/adma.201306281>, doi:<https://doi.org/10.1002/adma.201306281>. URL <https://onlinelibrary.wiley.com/doi/abs/10.1002/adma.201306281>
- [47] S. Kazim, M. K. Nazeeruddin, M. Grätzel, S. Ahmad, Perovskite as light harvester: A game changer in photovoltaics, *Angewandte Chemie International Edition* 53 (11) (2014) 2812–2824. arXiv:<https://onlinelibrary.wiley.com/doi/pdf/10.1002/anie.201308719>, doi:<https://doi.org/10.1002/anie.201308719>. URL <https://onlinelibrary.wiley.com/doi/abs/10.1002/anie.201308719>
- [48] G. Niu, X. Guo, L. Wang, Review of recent progress in chemical stability of perovskite solar cells, *J. Mater. Chem. A* 3 (2015) 8970–8980. doi:10.1039/C4TA04994B. URL <http://dx.doi.org/10.1039/C4TA04994B>
- [49] R. H. Mitchell, A. R. Chakhmouradian, P. M. Woodward, Crystal chemistry of perovskite-type compounds in the tausonite-loparite series, (sr1-2xnaxlax)tio3, *Physics and Chemistry of Minerals* 27 (8) (2000) 583–589. doi:10.1007/s002690000103. URL <https://doi.org/10.1007/s002690000103>
- [50] G. Dezanneau, A. Sin, H. Roussel, M. Audier, H. Vincent, Magnetic properties related to structure and complete composition analyses of nanocrystalline la1-xmn1-yo3 powders, *Journal of Solid State Chemistry* 173 (1) (2003) 216–226. doi:[https://doi.org/10.1016/S0022-4596\(03\)00027-6](https://doi.org/10.1016/S0022-4596(03)00027-6). URL <https://www.sciencedirect.com/science/article/pii/S0022459603000276>
- [51] A. M. Glazer, The classification of tilted octahedra in perovskites, *Acta Crystallographica Section B* 28 (11) (1972) 3384–3392. doi:10.1107/S0567740872007976. URL <https://doi.org/10.1107/S0567740872007976>
- [52] J. Verbeeck, O. I. Lebedev, G. Van Tendeloo, B. Mercey, sr_{1-x}tio₃(100)/(lamno₃)_m(srmno₃)_n layered heterostructures: A combined eels and tem study, *Phys. Rev. B* 66 (2002) 184426. doi:10.1103/PhysRevB.66.184426. URL <https://link.aps.org/doi/10.1103/PhysRevB.66.184426>
- [53] P. Norby, I. Andersen, E. Andersen, N. Andersen, The crystal structure of lanthanum manganate(iii), lamno3, at room temperature and at 1273 k under n2, *Journal of Solid State Chemistry* 119 (1) (1995) 191–196. doi:[https://doi.org/10.1016/0022-4596\(95\)80028-N](https://doi.org/10.1016/0022-4596(95)80028-N). URL <https://www.sciencedirect.com/science/article/pii/002245969580028N>

Supplementary Information for: "Optimizing Experimental Parameters for Orbital Mapping"

Manuel Ederer^a, Stefan Löffler^a

^a*University Service Centre for Transmission Electron Microscopy, TU Wien, Wiedner Hauptstraße 8-10/E057-02, 1040 Wien, Austria*



Email address: manuel.ederer@tuwien.ac.at (Manuel Ederer)

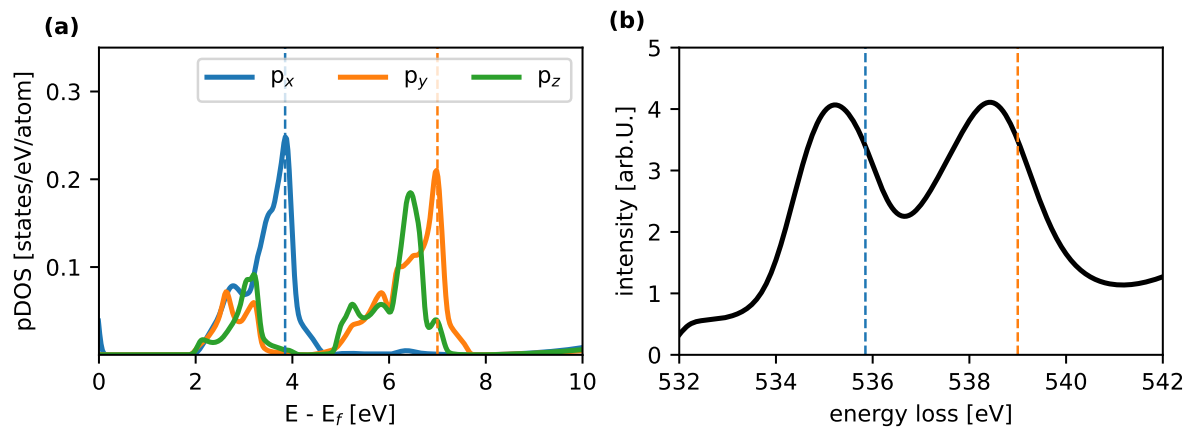


Figure S1: (a) DOS of rutile O. (b) Energy loss near edge spectrum of the O K-edge of rutile. Dashed lines mark the energy loss investigated in the main text.

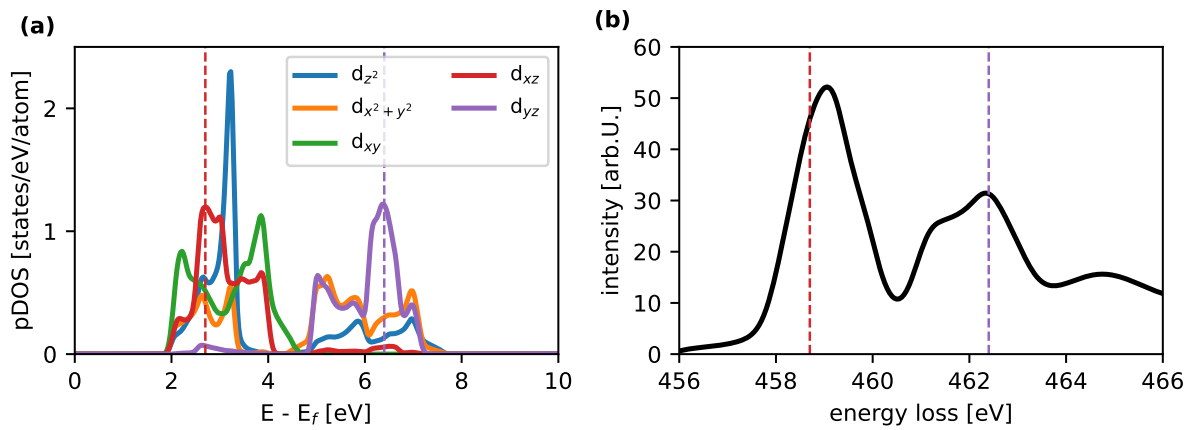


Figure S2: (a) DOS of rutile Ti. (b) Energy loss near edge spectrum of the Ti L₃-edge of rutile. Dashed lines mark the energy loss investigated in the main text.

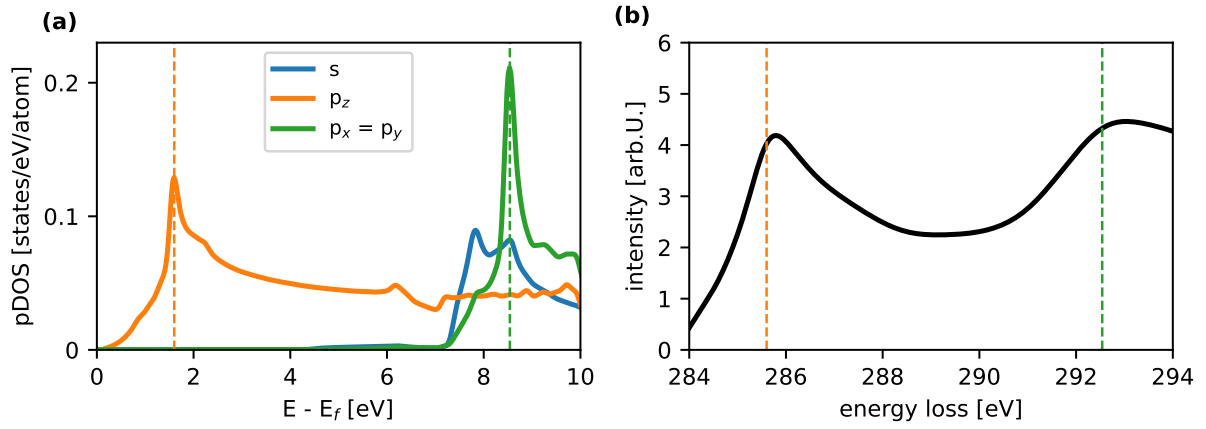


Figure S3: (a) DOS of graphite C. (b) Energy loss near edge spectrum of the C K-edge of graphite. Dashed lines mark the energy loss investigated in the main text.

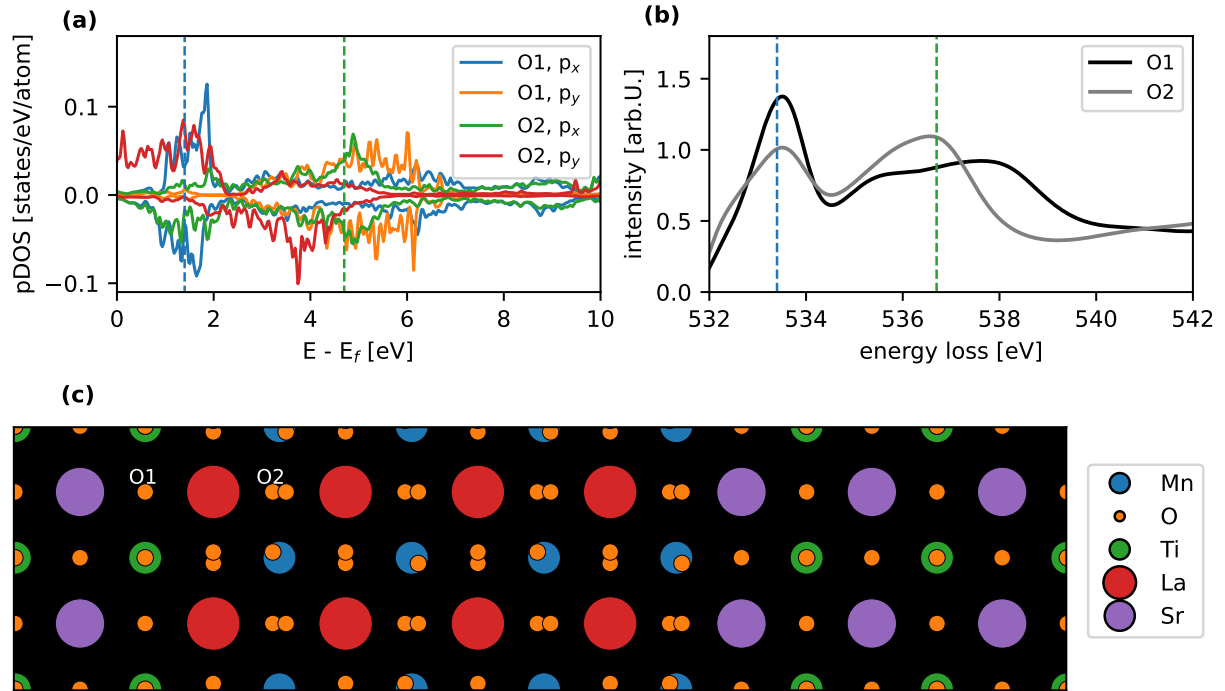


Figure S4: (a) Spin polarized DOS of two select O atoms in a SrTiO₃-LaMnO₃ interface. (b) Energy loss near edge spectrum of the O K-edge of the two select O atoms. Dashed lines mark the energy loss investigated in the main text. (c) Schematic of the SrTiO₃-LaMnO₃ interface in the [010] projection. The positions of the O atoms presented in (a) and (b) are marked with O1 and O2.

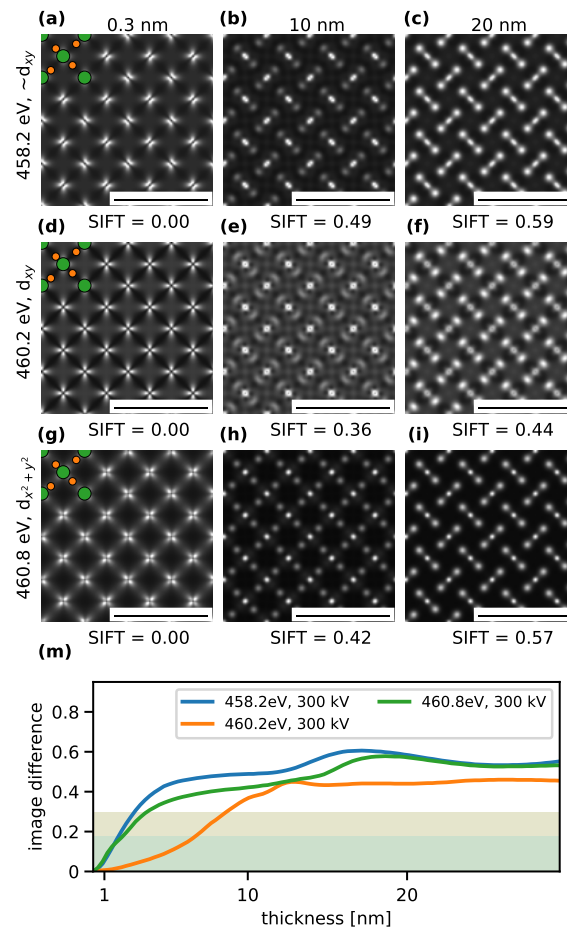


Figure S5: (a) - (i) Simulated energy-filtered TEM images of rutile in the [001] zone axis for the indicated sample thickness and energy loss. All scale bars indicate 1 nm. Green and orange dots mark the positions of Ti and O atoms, respectively. (m) SIFT image difference as function of sample thickness. All image differences are relative to the respective energy-filtered image for 0.3 nm sample thickness and 300 kV acceleration voltage.

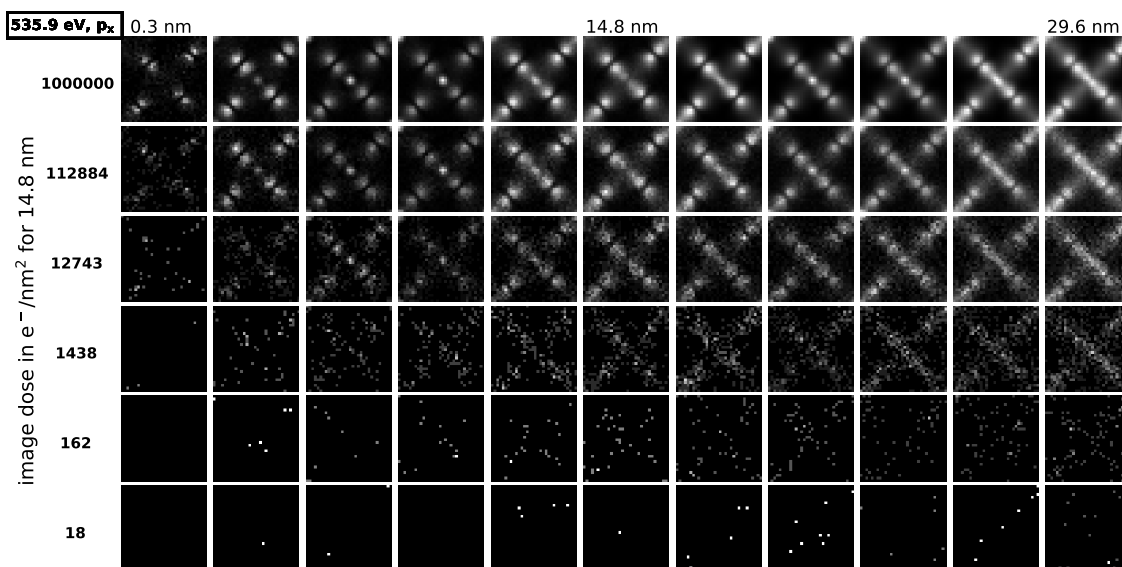


Figure S6: Simulated EFTEM images of a single rutile unit cell with added shot noise for varying sample thickness. The image dose values are given for the 14.8 nm thick sample. For the other cases, the image dose is scaled with the norm of the specific infinite dose image in order to simulate a constant incident dose.

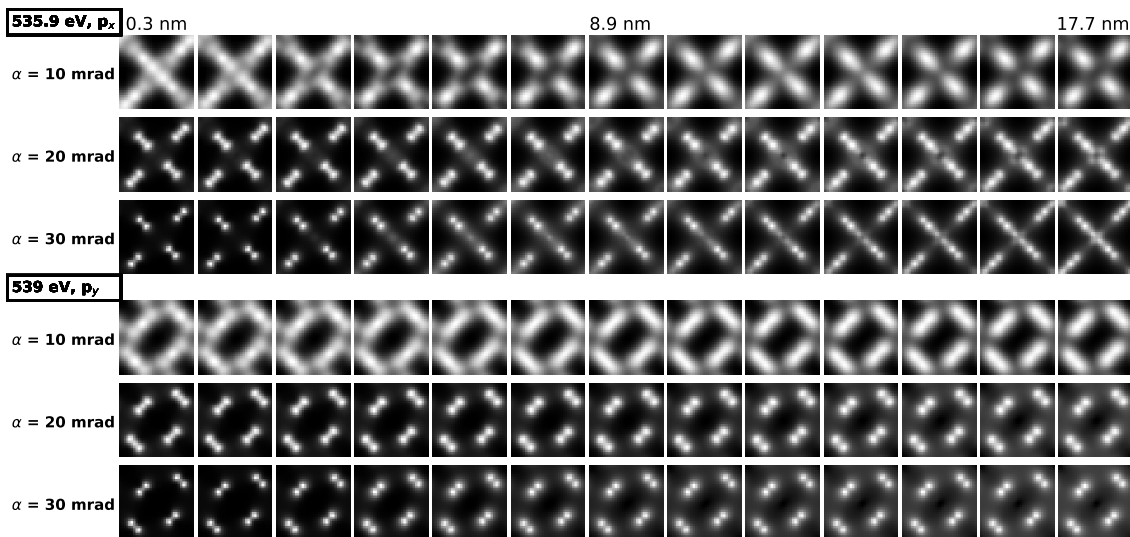


Figure S7: Simulated STEM-EELS maps of a single rutile unit cell for varying sample thicknesses and convergence semi-angles α . A collection semi-angle β of 50 mrad was used for all images.

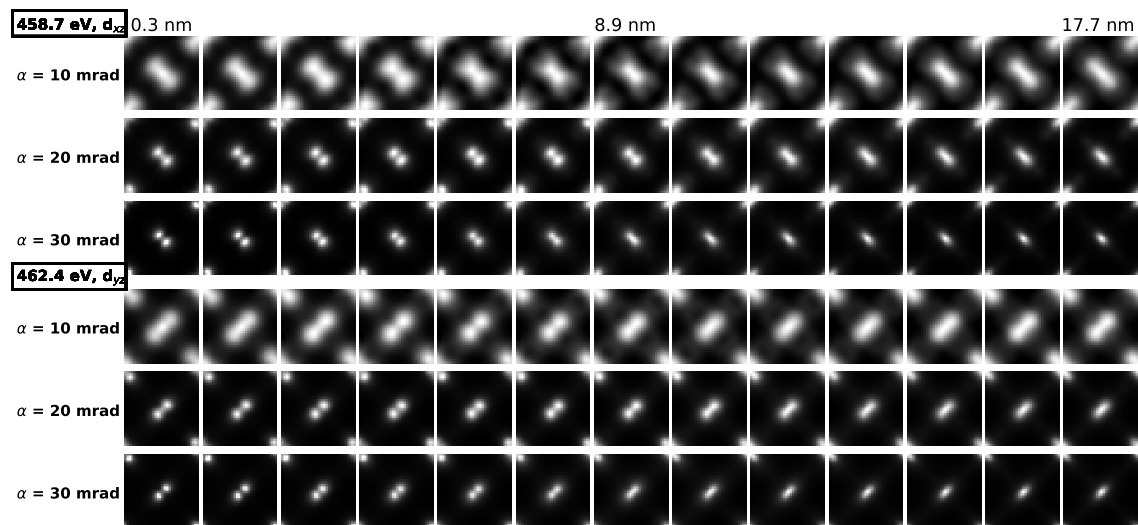


Figure S8: Simulated STEM-EELS maps of a single rutile unit cell for varying sample thicknesses and convergence semi-angles α . A collection semi-angle β of 50 mrad was used for all images.

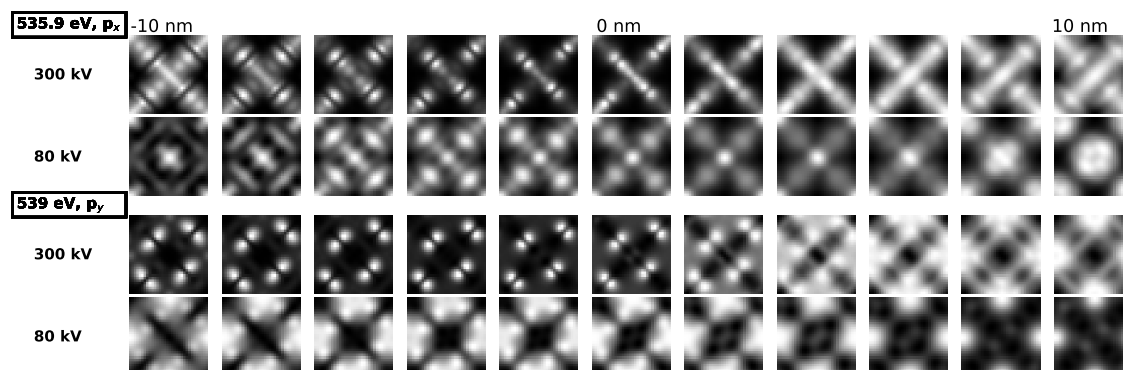


Figure S9: Simulated EFTEM images of a single rutile unit cell for varying sample thicknesses and defoci.

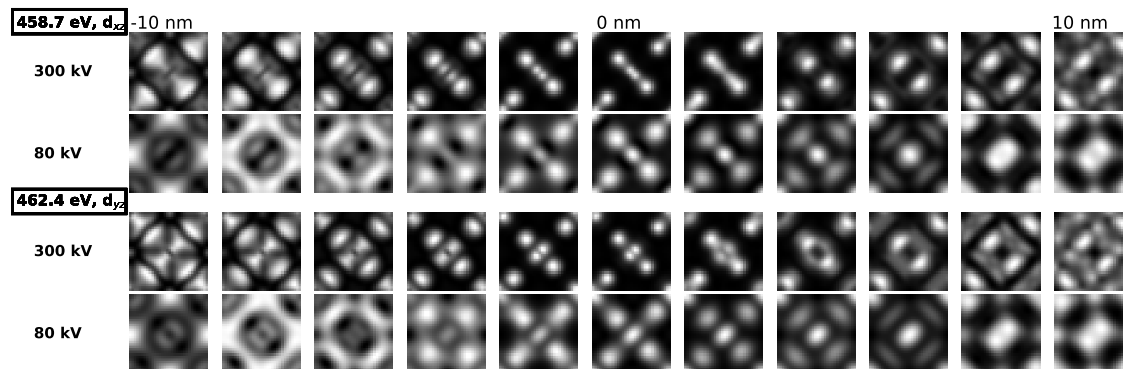


Figure S10: Simulated EFTEM images of a single rutile unit cell for varying sample thicknesses and defoci.

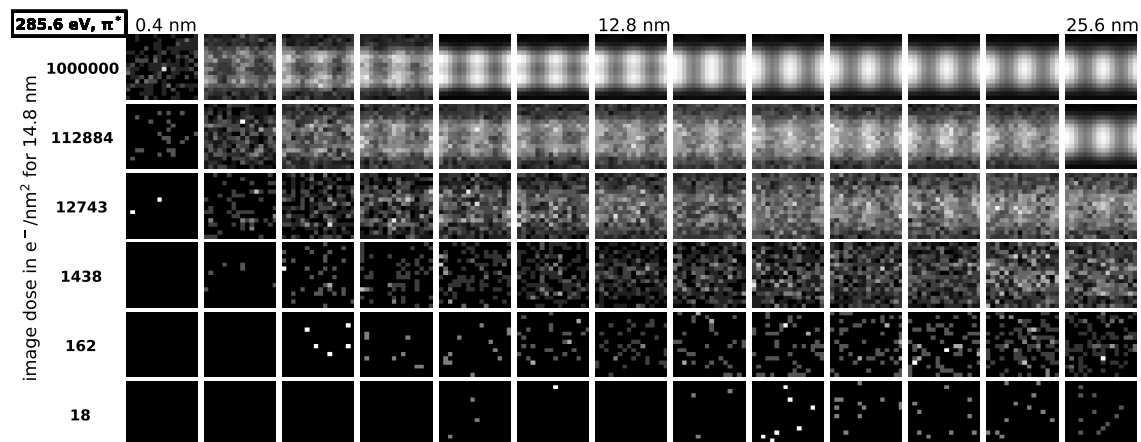


Figure S11: Simulated STEM-EELS maps of a single graphite unit cell with added shot noise for varying sample thickness. The image dose values are given for the 12.8 nm thick sample. For the other cases, the image dose is scaled with the norm of the specific infinite dose image in order to simulate a constant incident dose.

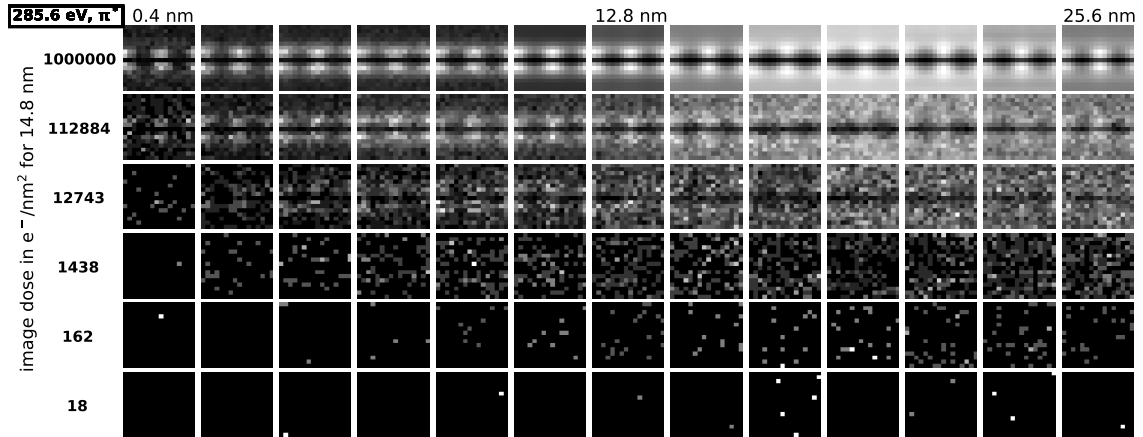


Figure S12: Simulated EFTEM images of a single graphite unit cell with added shot noise for varying sample thickness. The image dose values are given for the 12.8 nm thick sample. For the other cases, the image dose is scaled with the norm of the specific infinite dose image in order to simulate a constant incident dose.

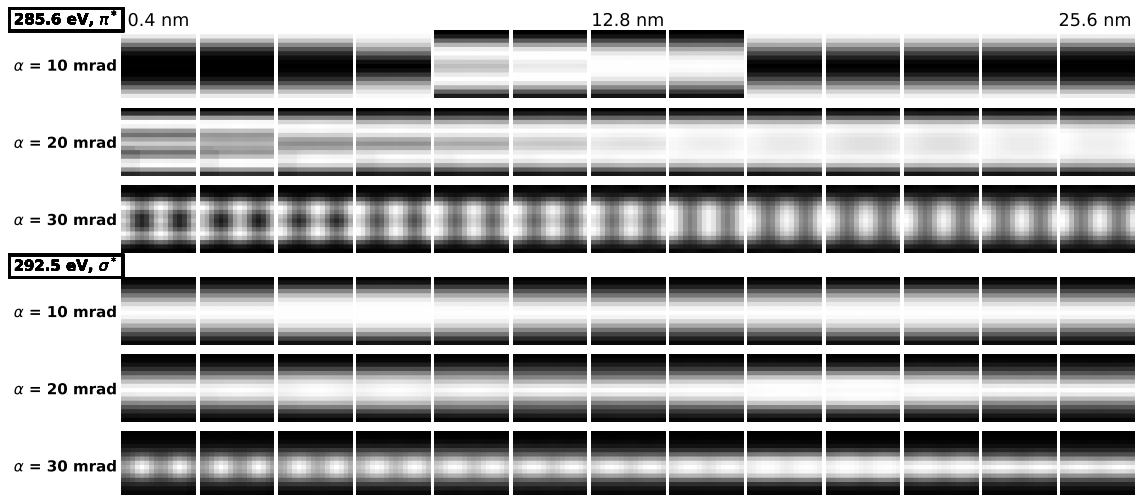


Figure S13: Simulated STEM-EELS maps of a single graphite unit cell for varying sample thicknesses and convergence semi-angles α . A collection semi-angle β of 50 mrad was used for all images.

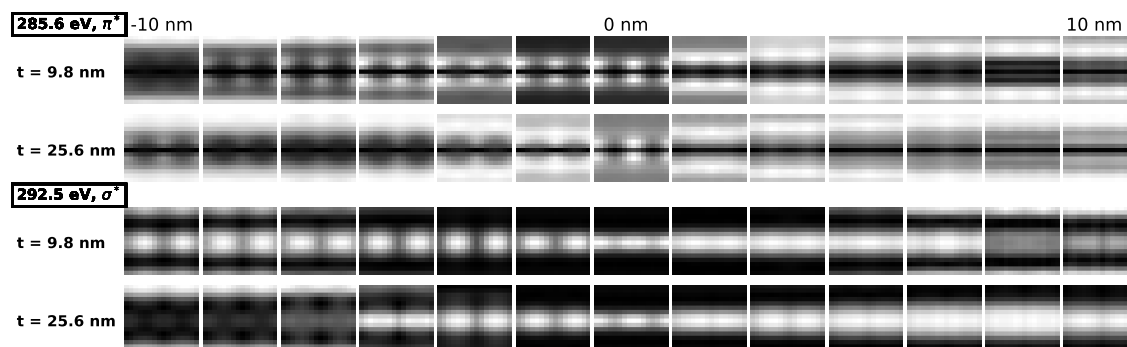


Figure S14: Simulated EFTEM images of a single graphite unit cell for varying sample thicknesses and defoci.

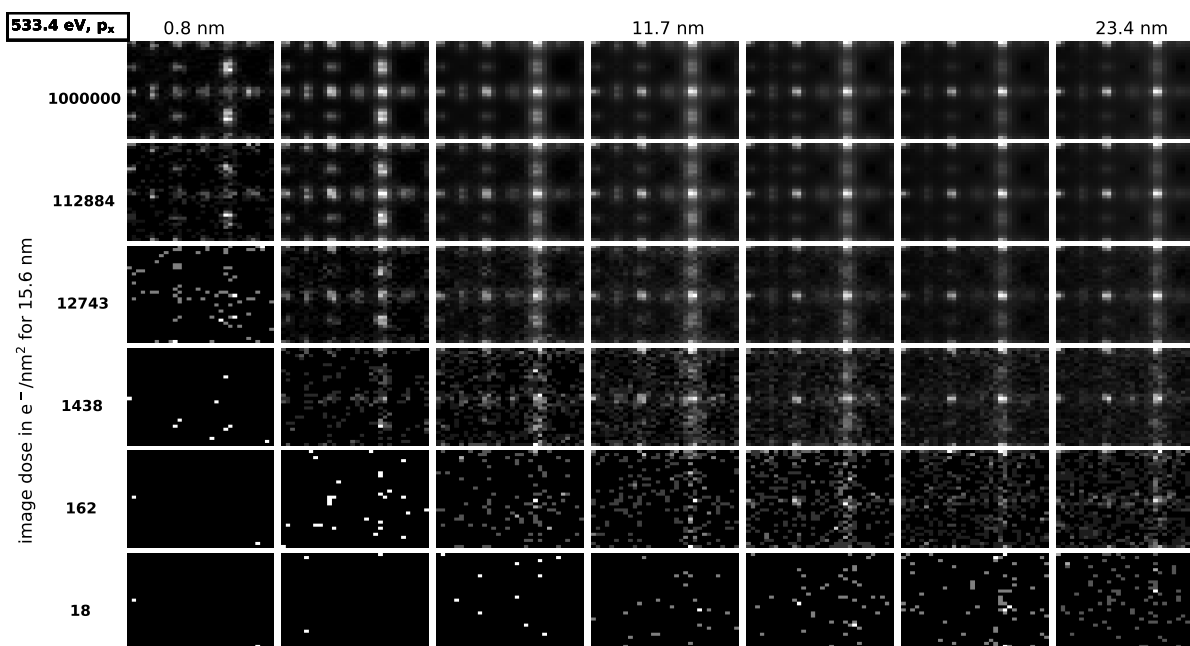


Figure S15: Simulated STEM-EELS maps of STO-LMO interface with added shot noise for varying sample thickness. The image dose values are given for the 16 nm thick sample. For the other cases, the image dose is scaled with the norm of the specific infinite dose image in order to simulate a constant incident dose.

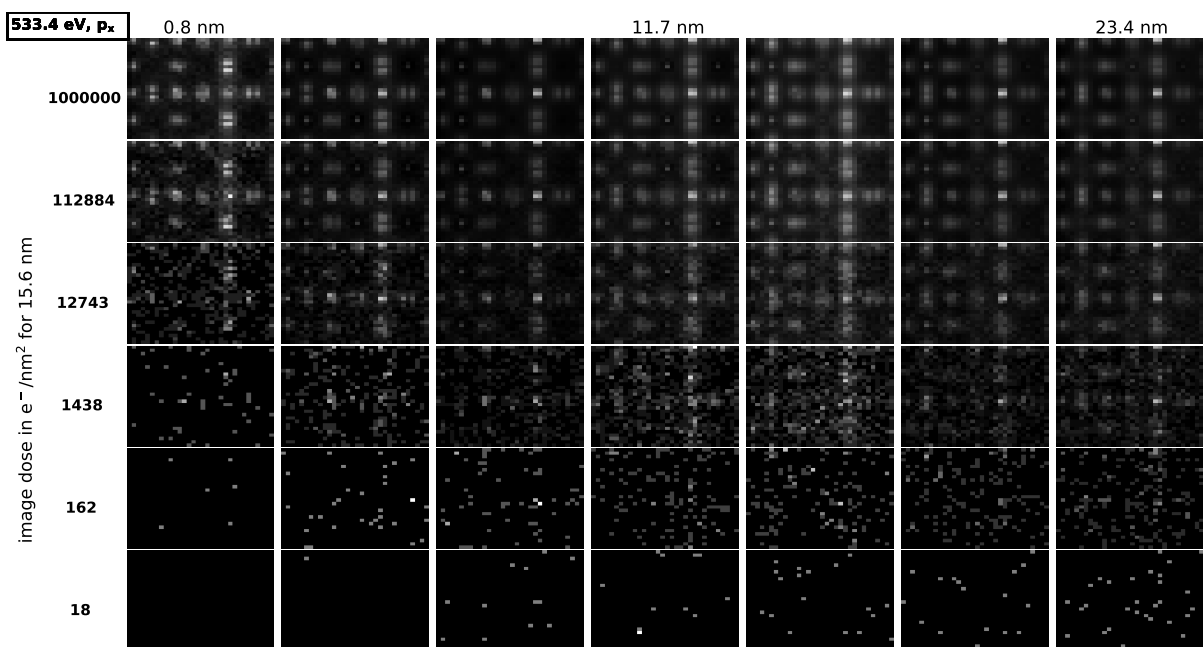


Figure S16: Simulated EFTEM images of STO-LMO interface with added shot noise for varying sample thickness. The image dose values are given for the 16 nm thick sample. For the other cases, the image dose is scaled with the norm of the specific infinite dose image in order to simulate a constant incident dose.

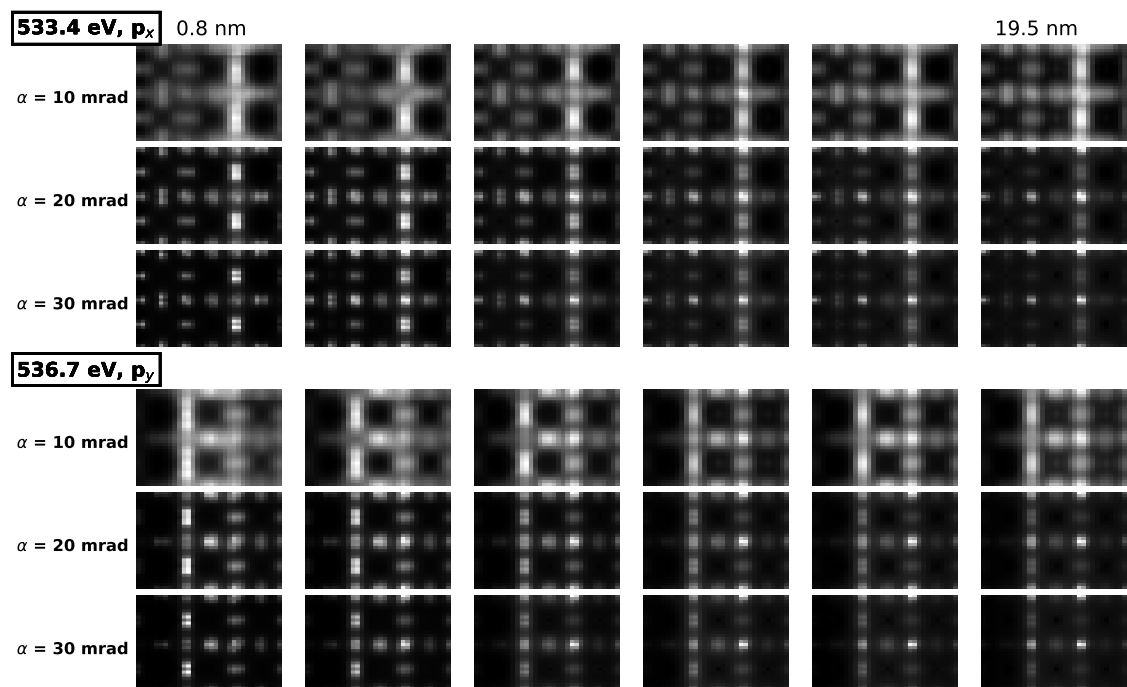


Figure S17: Simulated STEM-EELS maps of the STO-LMO interface for varying sample thicknesses and convergence semi-angles α . A collection semi-angle β of 50 mrad was used for all images.

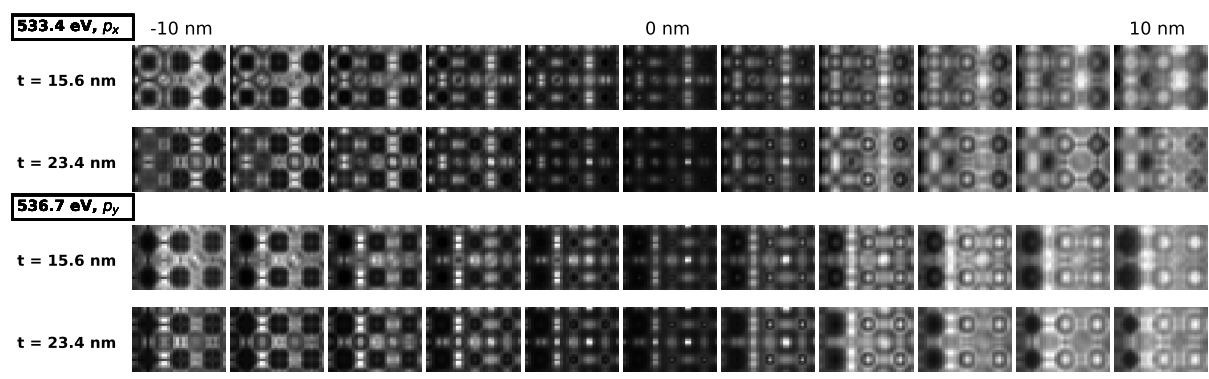


Figure S18: Simulated EFTEM images of the STO-LMO interface for varying sample thicknesses and defoci.